A new inventory of High Mountain Asia surging glaciers derived from multiple elevation datasets since the 1970s

Lei Guo[1], Jia Li[1], Amaury Dehecq[2], Zhiwei Li[1], Xin Li[3], Jianjun Zhu[1]

[1]School of Geo-science and Info-physics, Central South University, Changsha, 410083, China.

[2]Univ. Grenoble Alpes, IRD, CNRS, Grenoble INP, IGE, Grenoble, 38000, France.

[3]Institute of Tibetan Plateau Research, Chinese Academy of Sciences, Beijing, 100101, China.

Correspondence to: Jia Li (lijia20050710@csu.edu.cn)

Abstract. Glacier surging is an unusual instability of ice flow and inventories of surging glaciers are important for regional glacier mass balance studies and glacier dynamic studies. Glacier surges in High Mountain Asia (HMA) have been widely reported. However, the completeness of available inventories of HMA surging glaciers is hampered by the insufficient spatial and temporal coverage of glacier change observations, or by the limitations of the identification methods. In this study, we established a new inventory of HMA surging glaciers based on glacier surface elevation changes and morphological changes over four decades. Three elevation change datasets based on four elevation sources (the KH-9 DEM, NASA DEM, COP30 DEM, and HMA DEM) and long-term Landsat satellite image series were utilized to assess the presence of typical surge features over two time periods (1970s-2000 and 2000-2020). A total of 890 surging and 336 probably or possibly surging glaciers were identified in HMA. Compared to the most recent inventory of surging glaciers in HMA, our inventory incorporated 253 previously unidentified surging glaciers. The number and area of surging glaciers accounted for ~2.49% (excluding glaciers smaller than 0.4 km^2) and ~16.59% of the total glacier number and glacier area in HMA, respectively. Glacier surges were found in 21 of the 22 subregions of HMA (except for the Dzhungarsky Alatau); however, the density of surging glaciers is highly uneven. Glacier surges occur frequently in the northwestern subregions (e.g., Pamir and Karakoram), but less often in the peripheral subregions. The inventory further shows that surge activity is more likely to occur for glaciers with a larger area, longer length, and wider elevation range. Among glaciers with similar areas, the surging ones usually have steeper slopes than non-surging ones. The inventory and elevation change products of identified surging glaciers are available at: https://doi.org/10.5281/zenodo.7961207 (Guo et al., 2022).

Key words: High Mountain Asia, Surging glacier inventory, elevation change, KH-9, Digital Elevation Model (DEM)

1 Introduction

A surge is a glacier instability that translates into an abnormally fast flow over a period of a few months to years (Cogley et al., 2011). A surging glacier exhibits an active phase (surge) and a quiescent phase that may occur at quasi-periodic intervals (Jiskoot, 2011). During a glacier's surging phase, a large volume of ice mass is transported downstream at a higher-than-average speed. In the quiescent phase, a glacier returns to a slow-moving state, and gradually regains mass in the reservoir zone.

Previous studies pointed out that surge-type glaciers only represent ~1% of total glaciers (Jiskoot, 2011; Sevestre and Benn, 2015). However, glacier surges are far more than an occasional behavior in some specific regions, such as the Alaska-Yukon (Clarke et al., 1986), Svalbard (Jiskoot et al., 2000; Farnsworth et al., 2016), and Karakoram-Pamir (Bhambri et al., 2017; Goerlich et al., 2020; Guillet et al., 2022). Glaciers in these regions have experienced heterogeneous mass loss in the past decades (Hugonnet et al., 2021). Understanding how glacier surge activities impact the regional mass balance requires first the identification of surging glaciers. In recent years, substantial efforts have been made to understand the mechanisms of glacier surges, including models that account for hydrological controls (Kamb, 1987; Fowler, 1987), thermal controls (Fowler et al.,

40   2001; Murray et al., 2003), environmental factors (Hewitt, 2007; Van Wyk de Vries et al., 2022), friction state (Thøgersen et

41   al., 2019; Beaud et al., 2021), and enthalpy (Sevestre and Benn, 2015; Benn et al., 2019). These theories require comprehensive

42   validation by conducting detailed analysis on various glacier samples. To support related investigations, the distribution of

43   surging glaciers is needed as a starting point.

44   Generally, a surging glacier exhibits one or several of the following changes: extreme increase in flow velocity (by a factor of

45   10~1000 compared to the usual flow of non-surging glaciers), contrasting elevation change pattern (e.g. thickening in lower

46   reaches and thinning in upper reaches), rapid terminus advance, and surface morphological changes (deformed or looped

47   medial moraines, intense crevassing or shearing at the margins) (Jiskoot, 2011). The identification of surging glaciers can be

48   implemented based on the observation of these changes, e.g., by studying glacier surface morphology (Clarke et al., 1986;

49   Paul, 2015; Farnsworth et al., 2016), terminus position (Copland et al., 2011; Vale et al., 2021), glacier motion (Quincey et al.,

50   2011), or morphological-related indicators (e.g., normalized backscatter difference (Leclercq et al., 2021)). A surge-type

51   glacier, which refers to a glacier that possibly surged prior to the observation period, is generally identified by indirect

52   morphological evidence (without observed changes) (Goerlich et al., 2020). The visual interpretation of glacier surface

53   morphological changes is less calculative, but is prone to uncertainties due to the snow cover or the absence of supraglacial

54   moraine deformation (Jacquemart and Cicoira, 2022). To recognize sudden changes in glacier motion, a long-term flow

55   velocity time series is needed (Yasuda and Furuya, 2015; Round et al., 2017). Since the quiescent phase may last for decades

56   and the image sources for estimating flow velocity are limited, the strong changes in glacier motion associated with the surge

57   might be missed. In contrast, the recognition of a specific surface elevation change pattern can be a more reliable way to

58   identify surging glaciers, as it can remain visible for many years before and after a surge (Bolch et al., 2017; Zhou et al., 2018).

59   Besides, digital elevation models (DEMs) can satisfy the required spatio-temporal coverage with comparatively fewer datasets.

60   By combining observations of changes in glacier surface elevation, flow velocity, and morphological features, the

61   identification of surging glaciers could be more efficient and complete (Mukherjee et al., 2017; Goerlich et al., 2020; Guillet

62   et al., 2022). When conducting such studies on a large spatial scale or a long temporal scale, one should select the least time-

63   consuming but most effective identification method. In that case, datasets of elevation change covering many decades can be

64   helpful, especially if this information is combined with other observations such as flow velocity and morphological changes

65   (Guillet et al., 2022).

66   High Mountain Asia (HMA) is the most densely glacierized region in the world outside the polar regions. Within HMA, several

67   subregions are well known for the concentration of surging glaciers as well as the differing glacier mass balance in contrast to

68   the common thinning in other glacierized regions (Hewitt, 2005; Gardelle et al., 2013; Farinotti et al., 2020). Inventories of

69   surging or surge-like glaciers have been established for some subregions like the Karakoram (Bhambri et al., 2017), West-

70   Kunlun (Yasuda and Furuya, 2015), Pamir (Goerlich et al., 2020) and Tien Shan (Mukherjee et al., 2017; Zhou et al., 2021).

71   Sevestre and Benn (2015) presented the first global inventory of surging glaciers by reanalyzing historical reports from 1861

72   to 2013. However, it was compiled from various data sources (publications, reports, etc.) with inconsistent spatio-temporal

73   coverage, which makes it difficult to ensure accuracy and completeness. Vale et al. (2021) identified 137 surging glaciers

74   across HMA by detecting surge-induced terminus change and morphological changes from Landsat images obtained between

75   1987 and 2019. This number, however, is smaller than the numbers of previous subregional inventories (Bhambri et al., 2017;

76   Goerlich et al., 2020), because not all glaciers that surge do also advance. Guillet et al. (2022) presented a new surging glacier

77   inventory of HMA by identifying multiple glacier change features. In total, 666 surging glaciers were identified across HMA.

78   However, the glacier change observation period is shorter than two decades (2000-2018), and therefore some surging glaciers

79   with relatively long-repetition cycles may be missed.

80   In this study, we aimed to build a new inventory to include more surging glaciers within HMA based on glacier surface

81   elevation changes observations over four decades. A workflow was developed to obtain the historical glacier surface elevation

82   change from multiple DEMs, including the KH-9 DEM (1970s), NASA DEM (2000), COP30 DEM (2011-2014), HMA DEM

83   (2002-late 2016), and previously published elevation change datasets. The preliminary identified surging glaciers were divided
84   into three classes of confidence in surge detection. After that, this elevation-change based inventory was further completed
85   and corrected by identifying morphological changes in a time series of optical Landsat images between 1986 and 2021. Based
86   on the present inventory, the distribution and geometric characteristics of surging glaciers within HMA were statistically
87   analyzed, in order to demonstrate their spatial heterogeneity and geometrical difference from the normal glaciers.

88   **2 Study region**

89   High Mountain Asia consists of the Qinghai-Tibet Plateau and its surrounding regions, including the Karakoram, Pamir,
90   Himalayas, and Tien Shan. According to the updated Glacier Area Mapping for Discharge from the Asian Mountains
91   (GAMDAM2) glacier inventory, HMA hosts 131819 glaciers, covering a total area of ~99817 km^2 (Sakai, 2019). The Hindu
92   Kush Himalayan Monitoring and Assessment Programme (HiMAP) divided HMA into 22 subregions (Fig. 4) (Bolch et al.,
93   2019). Different subregions are influenced by different climate regimes, such as the South Asia monsoon, the East Asia
94   monsoons, and the westerlies (Bolch et al., 2012; Maussion et al., 2014). Glacier elevation changes across HMA were found
95   to be heterogeneous in the past decades (Gardelle et al., 2013; Brun et al., 2017; Shean et al., 2020). In particular, glaciers in
96   the Pamir-Karakoram-West Kunlun region had slightly positive or close to zero changes (Hewitt, 2005; Zhou et al., 2017;
97   Farinotti et al., 2020), while those in the Eastern Himalayas, Nyainqentanglha and Hengduan Shan mountain ranges
98   experienced substantial ice loss (Maurer et al., 2019).

99   **3 Datasets**

100   **3.1 Elevation Data**

101   The NASA DEM is mainly reprocessed from C-band SRTM (Shuttle Radar Topography Mission) data. Among the current
102   global DEMs, the NASA DEM has the shortest source data acquisition period (~11/02/2000~22/02/2000) (Farr et al., 2007).
103   Based on an improved production flow, the NASA DEM has a better performance than the earlier SRTM void-free product in
104   most regions (Crippen et al., 2016). The NASA DEM serves as the reference elevation source because its acquisition time,
105   2000, is suitable to divide the elevation change observations into periods before and after the beginning of the 21st century
106   with a moderate time span (one or two decades). Each tile of the product has an extent of 1°× 1° and a pixel spacing of 1 arc-
107   second (see Fig. 1a). In total, 313 tiles were downloaded from NASA LP DAAC
108   (https://e4ftl01.cr.usgs.gov/MEASURES/NASADEM_HGT.001/).
109   Another global DEM we used is the newly released Copernicus DEM GLO-30-DGED (i.e., COP30 DEM). The COP30 DEM
110   was edited from the WorldDEM™, which was generated based on the TanDEM-X mission. The global RMSE of the COP30
111   DEM is ±1.68 m (AIRBUS, 2020). Several studies have pointed out that this DEM is the most reliable open-access DEM to
112   date (Purinton and Bookhagen, 2021; Guth and Geoffroy, 2021). The source images of the COP30 DEM were mostly acquired
113   between 2011 and 2014, and therefore the COP30 DEM is suitable for representing the surface elevation in the 2010s. Like
114   the NASA DEM, the COP30 DEM has a pixel spacing of 1 arcsecond. Each tile of the product has an extent of 1°× 1°. In total,
115   313 tiles were downloaded through ESA Panda (https://panda.copernicus.eu/web/cds-catalogue/panda).
116   The High Mountain Asia 8-meter DEM (HMA DEM) was also utilized in this study. The HMA DEM was generated from
117   very high-resolution commercial optical satellite stereo images, including WorldView-1/2/3, GeoEye-1, and Quickbird-2
118   (Shean et al., 2020), through an automated photogrammetry workflow that is integrated with multiple error-control processes
119   (Shean et al., 2016). This DEM was originally produced for the mass balance estimation of HMA glaciers, so it covered most
120   of the glacierized regions in HMA. In total, 3598 DEM tiles were downloaded from the National Snow and Ice Data Center
121   (https://nsidc.org/data/HMA_DEM8m_MOS/versions/1). About 95% of the underlying stereo images were acquired between

2010 and 2016 (Fig. 1b). Due to the data voids and inconsistent acquisition time, the HMA DEM was taken as a supplementary elevation source to increase data coverage in the 2010s.

The Hexagon KeyHole-9 (KH-9) imagery was acquired in the 1970s. It is one of the earliest near-global satellite stereo image sources. The KH-9 imagery is characterized by a spatial resolution of 6-9 m, a wide coverage (130 km x 260 km), and a 70% forward overlap (Surazakov and Aizen, 2010). Many studies have utilized this imagery to estimate historical glacier surface elevation (Holzer et al., 2015; Zhou et al., 2017; Maurer et al., 2019). The KH-9 DEMs used in this study were generated through the automated ASPy pipeline (Dehecq et al., 2020). The methodology, validated in the European Alps and Alaska, achieved a vertical accuracy of ~5m (68% confidence level). For more details on the method of KH-9 DEM generation, we refer to Dehecq et al. (2020). In total, 238 DEMs with a spatial resolution of 48 m were generated from the KH-9 images acquired between 1973 and 1980 (see Fig. 1c). The KH-9 DEMs were utilized to represent the glacier surface elevation in the 1970s.

Several newly published elevation change datasets were also collected to document the surges that occurred between 2000 and 2020 (Brun et al., 2017; Shean et al., 2020; Hugonnet et al., 2021). We mainly used the elevation change results presented by Hugonnet et al. (2021) to extend the observation period to 2020, which has a spatial resolution of 100 m and a temporal interval of 5 years. Through the comparison of the multiple elevation change results, gross errors or false signals in elevation change from either our study or previously published results could be easily detected and removed.

3.2 Optical Satellite Images

To assist in the identification of surging glaciers, we also analyzed morphological changes associated with surges in multi-temporal optical satellite images. We mainly relied on the 1986-2021 Landsat imagery to capture morphological changes. We acknowledge that due to the 30 m spatial resolution, not all details of glacier surfaces are visible. We downloaded from the USGS (https://earthexplorer.usgs.gov) the false-color composite LandsatLook images with 30 m resolution (geo-referenced) that have good brightness contrast over snow/ice areas. Only images with less than 10% cloud cover were selected. In total, 7843 LandsatLook images from 148 frames were used (see Fig. 1d). We also utilized the very high-resolution (VHR) basemaps (Google/ESRI/Bing, etc.) as complements for surging feature identification. The fine resolution of these images allows us to visually check the possible morphological features caused by past surges.

3.3 Glacier inventory

In this study, we used the GAMDAM2 glacier inventory (Sakai, 2019) as a template for the inventory of surging glaciers, rather than the Randolph Glacier Inventory V6.0 (RGI6.0) (RGI Consortium, 2017). The GAMDAM glacier inventory has included many small glaciers that are missed in RGI6.0, and provides a more accurate glacier extent by also excluding rock outcrops, seasonal snow, and shaded areas (Nuimura et al., 2015). Since the GAMDAM2 inventory only contains the glacier polygon vectors, we calculated the geometric and topographic attributes for each glacier in a way similar to that of RGI6.0. The maximum glacier centerline was calculated through the Open Global Glacier Model (OGGM) (Maussion et al., 2019). The attributes were used to analyze the geometric characteristics of surging glaciers.

4 Methodology

4.1 Estimation of glacier surface elevation change

The four kinds of DEMs have different coordinate references, vertical references, and data formats. Firstly, all DEMs were converted to float GeoTiff format. For datasets with quality files (the NASA DEM and the COP30 DEM), the DEMs were preprocessed to mask out the pixels of low quality. Pixels in the COP30 DEM with height error larger than 2.5 m or within the attached water body mask were excluded. The NASA DEM was directly masked with the attached water mask file.

161 Subsequently, the coordinate system, map projection, and vertical reference of all DEMs tiles were set as the WGS84
162 coordinate system, an Albers Equal Area projection customized for HMA regions (Shean et al., 2020) and the WGS84 ellipsoid.
163 The reprojection was performed using cubic resampling. The glacier surface elevation changes during 2000-2010s were
164 derived by subtracting the NASA DEM from the COP30 DEM and HMA DEM, and those during 1970s-2000 were derived
165 by subtracting the KH-9 DEM from the NASA DEM.

166 An automated DEM differencing workflow for large-scale glacier surface elevation change estimation was developed based
167 on the *demcoreg* package presented by Shean et al. (2019). The workflow integrates multiple DEM co-registration approaches,
168 such as a polynomial fit of tilt error, and other adaptive outlier removal approaches that were operated based on observations
169 over stable regions. Hence, a mask that excluded the water bodies and glacierized regions was generated in advance. Before
170 differencing, the two DEMs need to be co-registered, because a small geolocation shift can result in considerable elevation
171 change errors in high-mountain regions. The efficient analytical DEM co-registration method presented by Nuth and Kääb
172 (2011) was used to eliminate a relative geolocation shift (horizontal and vertical) between DEMs. This method assumes the
173 geolocation shift vectors of all DEM pixels are identical. However, for the global DEM products like the NASA DEM and the
174 COP30 DEM, a DEM tile was usually merged from multiple DEM patches, and the geolocation shift vectors at different parts
175 of the DEM tile may be different. In view of this problem, we developed a block-wise version of the analytical DEM co-
176 registration method to reduce the impacts of the non-uniform geolocation errors of a DEM tile. Each DEM tile was divided
177 into m×n blocks, and DEM shifts were estimated for each block. Then, the m×n groups of shift parameters were merged into
178 one group of shift parameters through a cubic interpolation. Technically, the estimated shift parameters become increasingly
179 representative as the block size decreases. However, the fitting of shift parameters requires a certain number of samples. The
180 final block size was set to 300×300 pixels to reach the best balance between the representativeness and estimation accuracy of
181 the shift parameters. Besides, we found that the block-wise co-registration method could result in wrong fitting of shift
182 parameters over flat regions. To deal with this, a threshold of mean slope (10°) was set to classify the DEMs into the flat and
183 the hilly terrain, and the original global co-registration method (Nuth and Kääb, 2011) was applied to the flat areas.

184 Due to the residual orbital error of satellite images, the elevation difference (dH) maps often showed planimetric trends. This
185 type of systematic error was corrected by subtracting from the elevation change a quadratic polynomial model which was fitted
186 to the observations in assumed stable regions (Li et al., 2017). Besides, due to the jitter of the SAR antenna and optical mapping
187 camera, the elevation difference maps often showed stripes (i.e., band-like artifacts) (Yamazaki et al., 2017). To eliminate the
188 stripes, the elevation difference map was converted to the frequency domain through a Fast-Fourier-Transform method. Since
189 the cyclic values have a high frequency in the power spectral density map, a threshold of frequency was set to separate the
190 stripes components from the normal elevation differences. The de-stripping was completed after the backward transformation.
191 Finally, pixels for which the elevation difference was larger than three times the standard deviation of all pixels were
192 considered as outliers and removed.

193 The radar penetration into snow and ice can result in elevation biases of several tens of meters over glaciers. We adopted a
194 two-step procedure to reduce the radar penetration bias in the final elevation change results. First, we used the DEM
195 differencing workflow mentioned above to subtract the NASA DEM from the SRTM-X DEM. The elevation differences over
196 glacierized area were regarded as the penetration difference between X-bands and C-bands. Secondly, we fitted a polynomial
197 function of degree three to the relationship between glacial elevation difference and altitude, which accounts for the fact that
198 penetration increases at higher altitude, in drier snow and ice conditions. The estimated radar penetration biases were removed
199 from the COP30 DEM to NASA DEM difference over glaciers. For the dH results calculated by differencing the NASA DEM
200 and optical DEMs (e.g. the HMA and KH-9 DEM), the penetration difference of X- and C- bands was multiplied by 2 to
201 account for the fact that the penetration depth of C-band is approximately twice that of X-band in dry snow (Rott et al., 1993;
202 Abdel Jaber et al., 2019; Fan et al., 2022) and then subtracted from the related results.

203 In total, our elevation change observations covered ~92% of the total glacier area within HMA in 2000-2020, and ~77% in
204 1970s-2000. Gaps in observations were mainly due to: 1) data voids and incomplete coverage of the original DEMs tile, which
205 was the main cause for the KH-9 DEMs and HMA DEM related results; 2) gross error removal during the elevation change
206 calculations, which led to the scattered holes in the COP30 DEM related results.

4.2 Surging glacier identification

208 The identification of surging glaciers in this study was divided into three steps. First, we generated a raw inventory of surging
209 glaciers through the qualitative interpretation of multi-temporal elevation changes. Then, the visual identification of
210 morphological changes was carried out for the identified surging and surge-like glaciers. This procedure can further confirm
211 the surges or correct the false identifications based on glacier elevation changes (Guillet et al., 2022). The identified results
212 were checked again by careful inspection on VHR images, and by comparing them with existing surging glacier inventory.
213 Besides, the surging tributaries were separated from the non-surging glacier trunk at this step.

4.2.1 Identification through elevation changes

215 A typical glacier surge cycle can be divided into three phases (Jiskoot, 2011): 1) the build-up phase, characterized by
216 remarkable thickening in the upper reaches; 2) the active phase, characterized by remarkable thinning in the upper reaches and
217 thickening in the lower reaches; 3) the post-surge phase, characterized by strong down-wasting in the lower reaches. The
218 classical method of identifying surging glaciers is to recognize the combination of marked upper thinning and lower thickening
219 in the longitudinal direction. However, to distinguish the surging glaciers in the build-up or post-surge phase, careful
220 comparison with surrounding glaciers is required, which is difficult to be carried out with a mathematical index. In this study,
221 we established a three-class indicator to distinguish the surge possibility through the visual recognition of continuous glacier
222 elevation changes over an area larger than 0.04 km^2 that are higher than the thresholds listed below:
223   I) "verified":
224   - a) obvious thickening in lower reaches (e.g., +30 m);
225   - b) contrasting upper-thinning (e.g., -20 m) and lower-thickening (e.g., +20 m);
226   - c) contrasting upper-thickening (e.g., +20 m) and lower-thinning (e.g., -30 m);
227   - d) severe thinning in the lower reaches (two times stronger than that of the normal glaciers, or comparable to the
228   ablation of adjacent "verified" surging glaciers);
229   II) "probable":
230   - e) moderate upper thinning (e.g. -15m) and lower thickening (e.g., +15m);
231   - f) only moderate thickening in the middle reaches (e.g., +15m);
232   III) "possible":
233   - g) only moderate thickening at the terminus (e.g., +15m);
234   - h) only strong thinning in the lower reaches (one time stronger than adjacent normal glaciers).
235 Note that the specific values of elevation change mentioned above were for information only. Because of the diversity in the
236 regional elevation change patterns under different climate or topographic conditions, the thresholds may vary spatially.
237 The identification of surging glaciers was conducted separately in the two observation periods (1970s-2000 and 2000-2020).
238 The sub-inventory covering the period 1970s-2000 was generated based on the dH results of the NASA DEM – KH-9 DEM.
239 For the sub-inventory covering the period 2000-2020, the dH datasets contain the COP30 DEM – NASA DEM, the HMA
240 DEM – NASA DEM, and three previously published elevation change datasets from Brun et al. (2017), Shean et al. (2020)
241 and Hugonnet et al. (2021). Within each observation period, each glacier was labeled with its possibility level of surging and
242 elevation change pattern in the attribute table. For example, the label "I-c" means this glacier was classified as a "verified"

243   surging glacier because contrasting upper-thickening and lower-thinning patterns were observed in the corresponding period.

244   Figure 2 shows an example of surging glacier identification result.

4.2.2 Identification through morphological changes

246   Long-term Landsat images (acquired between 1986 and 2021) were utilized to investigate the morphological changes of the

247   three types of potential surging glaciers identified from elevation change. Within each Landsat acquisition frame, all

248   Landsatlook images of different dates (acquired from 1986 to 2021) were merged into an animated time-series image. Based

249   on the animated image, we are able to identify morphological changes. Due to the moderate resolution of Landsat images, only

250   three types of feature changes were utilized as criteria for identifying glacier surges: terminus position change, looped moraine

251   changes, and medial moraine changes. Similarly, we assigned a two-level index to each morphological change to indicate our

252   confidence in the identification, which was defined as follows:

253   1) terminus advance:

254   T1): strong terminus advancing (e.g., over 500 m);

255   T2): slight terminus advancing (e.g., 0~500 m);

256   2) looped/medial moraine change:

257   M1): fast formation/vanishment of the looped moraine, or obvious distortion of the medial moraine;

258   M2): slow formation or vanishment of the looped moraine, or slight shape changes of existing looped moraine, or

259   slight distortion of the medial moraine.

260   Each of the three kinds of morphological changes was individually qualified and labeled in the attribute table. All criteria used

261   for identifying surging glaciers were listed in Table 1.

4.2.3 Generation of surging glacier inventory

263   Through the above identification steps, in total five indicators were compiled to describe the changes of possible surging

264   glaciers. The two sub-inventories based on elevation change maps (section 4.2.1) were first merged following the principle of

265   possibility, i.e., if a glacier was identified as a surging glacier in both periods but associated with different indicators, its

266   indicator in the final inventory was taken from the indicator having a higher possibility. The possibility of indicators follows

267   the order: "verified" > "probable" > "possible". For example, a glacier identified as a "verified" surging glacier in the period

268   1970s-2000, and identified as a "probable" surging glacier in the period 2000-2010s was classified as a "verified" surging

269   glacier. This intermediate inventory was further merged with the inventory based on morphological indicators to determine

270   the final indicator of surge possibility. The "probable" or "possible" class was changed to a class with higher possibility (e.g.,

271   from "probable" to "verified") only if an obvious morphological change was observed (i.e., "T1" type of terminus advancing

272   or "M1" type of looped/medial moraine change).

273   We think the advancing glaciers usually have such features: 1) only thickened in a small area at the terminus, without

274   contrasting upper thinning; 2) the advancing distance is relatively short (Lv et al., 2019, 2020; Goerlich et al., 2020). These

275   features correspond to the "III-g" type of elevation change, and the "T1" type of terminus advance. Therefore, if a glacier only

276   shows these two kinds of changes, it will be qualified as an advancing glacier, rather than a surging glacier.

277   For glaciers, in which a tributary surged but the main trunk did not show any features of a surge, such as Biafo, Fedchenko, or

278   Panmah glaciers (Hewitt, 2007; Goerlich et al., 2020; Bhambri et al., 2022), we separated the surging tributary from the trunk.

279   A tributary will be considered as an individual surging glacier in the following conditions: the transition of contrasting

280   elevation change is located in this tributary and the mass contributed by this tributary to the glacier trunk is relatively small.

281   In that case, we manually edited the outline to separate the tributary from the glacier complex. This kind of surge was also

282   marked by the attribute "trib_surge".

In the final step, we inspected the identified surging glaciers on VHR imagery. The inspection aimed to remove wrong identifications caused by some false signals, such as the severe lower-thinning in a lake-terminating glacier and remarkable surface heightening caused by nearby landslides. We also refined our inventory after careful comparison with inventories presented by Guillet et al. (2022), Goerlich et al. (2020), and Bhambri et al. (2017).

4.3 Estimation of the uncertainty

The reliability of surging glacier identification is directly related to the accuracy of glacier surface elevation change. Assuming the uncertainties in elevation difference are similar over glacierized and stable areas, we evaluated the uncertainties of glacier elevation difference based on elevation difference observations in stable areas, whose true values are zeros. Here we adopted the normalized median absolute deviation (NMAD) as the indicator of uncertainty of elevation difference, which is less sensitive to outliers and can be deemed as a better proxy of the standard deviation for dH in mountainous area (Höhle and Höhle, 2009; Li et al., 2017). The NMAD is calculated as follow:

$$\text{NMAD} = 1.4826 \times median(|\Delta h_i - median(\Delta h)|) \tag{1}$$

where Δh is the elevation difference and the subscript i denotes the index of the pixel.

In this study, uncertainties in glacier elevation change are caused by uncertainties in the elevation difference and in the penetration depth. Since the penetration depth was also estimated from a DEM difference (SRTM-X DEM – NASA DEM), its uncertainty can also be evaluated through the NMAD. Assuming that these two kinds of uncertainties are uncorrelated, the uncertainty of the glacier elevation change is estimated through the error propagation law:

$$\delta_{dH} = sqrt(\delta^2_{elev\_diff} + n \times \delta^2_{pene}) \tag{2}$$

Where $elev\_diff$ means the elevation difference, and $pene$ means the penetration depth difference between C-band and X-band SRTM. The coefficient n is the factor between the C- and X-band penetration depth, which is 1 for the results of COP30 DEM – NASA DEM and 2 for the results of KH-9/HMA DEM – NASA DEM.

5 Results

5.1 Identified surging glaciers

A total of 1226 surge-related glaciers across the HMA were identified based on the elevation changes and morphological changes. The identified surge-related glaciers consisted of 890 'verified' surging ones, 208 'probable' ones, and 128 'possible' ones. A total of 175 surging tributaries were identified in 86 glacier complexes. When merging the identification results of the two periods, we found that a considerable proportion of identified surging glaciers were simultaneously recognized in both periods. This makes our inventory more reliable since a surging glacier could exhibit different kinds of changes in different periods. For example, 26 probable and 51 possible surging glaciers identified during 2000-2020 turned out to be "verified" surging glaciers during 1970s-2000. Meanwhile, 60 "probable" and 21 "possible" surging glaciers identified during 1970s-2000 turned out to be 'verified' surging glaciers during 2000-2020. Due to the almost complete coverage of elevation change observations, we were able to classify almost all glaciers in HMA. Table 2 shows the number of surging glaciers identified from two periods of elevation changes and morphological changes. Due to the incomplete coverage of KH-9 DEMs, 103 identified surging glaciers have no observations during the period 1970s-2000. The data voids in KH-9 DEMs may be one of the reasons why fewer surging glaciers were identified in this period. In the following text, the "probable" and "possible" classes were deemed as surge-like glaciers, and only the "verified" surging glaciers were used for analysis and comparison throughout the rest of this study.

5.2 Distribution of surging glaciers

Surging glaciers were identified in 21 subregions of HMA (except for the Dzhungarsky Alatau); however, the spatial density of identified surging glaciers varies between different subregions (Fig. 3). Glacier surges are common in the northwestern regions, sporadic in the inner regions, and scarce in the peripheral regions. Figure 4 and Table 2 show the ratios of surging glacier number and area in each subregion. Considering the area of the smallest identified surging glacier is 0.42 km^2, we only counted glaciers larger than 0.40 km^2 in the glacier number ratio. When conducting statistical analysis, the surge-like glaciers were excluded from the dataset. Besides, a surging tributary was regarded as an individual glacier. The number (890) and area (16556.42 km^2) of identified surging glaciers accounted for ~2.49% and ~16.59% of the total glacier number and glacier area in HMA, respectively.

Among the 22 subregions, the Karakoram is the largest cluster of surging glaciers. In total 354 surging and 128 surge-like glaciers were identified in the Karakoram. The number and area of verified surging glaciers in the Karakoram accounted for 39.80% and 47.90% of the total identified surging glaciers within HMA. We found that more than half of the tributary surges (101) occurred in the Karakoram, where large glaciers are much more developed than in other regions. In the Karakoram, although surging glaciers account for only 8.59% of the total glacier number, their area occupied 39.48% of the total glacierized area. The Pamirs, composed of the Eastern Pamir, Western Pamir, and Pamir Alay, hosts 249 surging glaciers and 128 surge-like glaciers. About 27.74% of the glacier area in the Eastern and Western Pamir belongs to surging glaciers. We also found 28 surging tributaries in 15 glacier complexes in the Pamirs. Surging glaciers are also common in the Western Kunlun. In total 82 surging and 47 surge-like glaciers were identified in the West Kunlun, representing 30.48% of the total glacier area. The Central Tien Shan has the fourth-largest surging glacier area. In total 59 surging glaciers were identified in the Central Tien Shan, covering 12.93% of the total glacier area. The Karakoram, Pamirs, West Kunlun, and Central Tien Shan host ~83% of the surging glaciers across HMA. Figure 5 shows the distribution of identified surging and surge-like glaciers in these four regions.

Within interior HMA subregions (including the Tibetan Interior Mountains, Eastern Kunlun Shan, and Tanggula Shan), identified surging glaciers represent less than 2% of the total number but nearly 15% of the total glacier area. Glacier surges in these regions occurred in a few watersheds. Similar localized surging glacier clusters were also found in the Nyainqentanglha, Northern, and Western Tien Shan, and Central Himalaya, but the corresponding area ratios are much lower. In these regions, our inventory covers dozens of surging glaciers, which were rarely reported before. Figure 6 shows some samples of identified surging glaciers in these regions.

5.3 Geometric characteristics of surging glaciers

In this part, only the surging glaciers and non-surging glaciers are taken for analysis. The surge-like glaciers are not included. All glacier samples in the surging and non-surging classes are larger than 0.40 km^2.

We divided all glaciers into 9 classes according to their area, and calculated the ratios of surging glacier number and area in each class. As shown in Fig. 7 and Table 4, surging glaciers were found in all classes. Both the ratios of surging glacier area and number became increasingly high as the glacier size increased, except for the last class. Surging glaciers with an area of 1-50 km^2 occupy 82% of all surging glaciers. For the three classes in which glaciers are larger than 50 km^2, the ratios of surging glaciers area and number were about 52% and 54%, respectively. In particular, 2 of 6 very large glaciers (the Siachen glacier and the Hispar glacier) surged during our observation periods.

When comparing the geometric characteristics of the surging glaciers and non-surging glaciers, we selected samples in the following way: for each surging glacier, we selected 10 non-surging glacier samples that have the closest area but from an arbitrary region; and then we randomly sampled 3 out of the 10 selected non-surging glaciers. This is to minimize the discrepancy resulting from the sample differences. There are two reasons for doing so. First, the gap between the sample

361 numbers is huge (~35000 non-surging vs. 890 surging). Second, a high proportion of non-surging glaciers are very small

362 glaciers. The final selected 890×3 non-surging glaciers formed the reference group.

363 Figure 8 illustrates the comparisons between the basic geometric properties of surging and non-surging glaciers. The sampling

364 strategy mentioned above was also utilized here. If we directly compare the surging glaciers with all non-surging glaciers, we

365 will find that surging glaciers generally have a larger area, wider elevation range (i.e., the highest glacier surface elevation

366 minus the lowest), and longer flow line (Figs. 8a-c). Taking the median values as the candidates, the quantitative comparisons

367 are 7.3 km^2 (surging) vs. 0.87 km^2 (non-surging) for glacier area, 1534 m vs. 642 m for elevation range, and 6695 m vs. 1854

368 m for maximum glacier length, respectively. In terms of mean surface slope and median elevation, the values of the surging

369 glaciers are less spread out than the non-surging glaciers. However, the median values of the two kinds of glaciers are very

370 close (see Figs. 8d and 8e). If we took the non-surging glaciers in the reference group for comparison, the discrepancies

371 between the two kinds of groups on these geometric properties became much more different. As shown in Fig. 9a, the similar

372 boxplots of the reference group and surging glacier samples proved that our sampling strategy successfully corrected the bias

373 in area between surging and non-surging glaciers. The gaps between the surging and non-surging glaciers (reference group) in

374 the glacier area (7.3 km^2 vs. 7.0 km^2), elevation range (1534 m vs. 1180 m), and glacier length (6695 m vs. 5560 m), are much

375 smaller. More importantly, the mean slope of the glaciers in the reference group becomes smaller than that of the surging

376 glaciers.

377 The correlation between different glacier geometric properties was analyzed through the bivariate scatterplots (see Fig. 9).

378 Among the glacier area, glacier length, and glacier surface elevation range, any two of them have an apparent positive

379 correlation. The glacier mean slope has a moderate correlation with glacier area, length, and elevation range as they are auto-

380 correlated. By contrast, glacier median elevation has little correlation with these parameters. The correlation of any two

381 geometric properties makes little difference between surging and non-surging glaciers. All variables mentioned above are

382 embedded in the attribute table of the published inventory. Detailed descriptions of these variables can be found in Table 5.

383 **6 Discussion**

384 **6.1 Uncertainty analysis**

385 Figure 10 shows the uncertainties in four kinds of elevation difference observations and three kinds of glacier elevation change

386 observations. The four kinds of elevation difference observations include three kinds of DEM difference observations and one

387 kind of radar penetration depth difference observation. The uncertainties in glacier elevation change originated from the DEM

388 difference and from the radar penetration depth difference. For each kind of elevation difference observation, the average

389 uncertainty (NMAD) is generally smaller than 4.50 m, and the uncertainty of the penetration depth difference is the smallest.

390 Due to the large distortion in the KH-9 images, the NASA DEM – KH-9 DEM results had the highest uncertainties. In general,

391 the uncertainties of our elevation change results are acceptable. Compared with the typical surface elevation change resulting

392 from a glacier surge (tens to hundreds of meters), the uncertainties are very small. For example, a large uncertainty in the KH-

393 9 DEM related elevation change observation (say 8.00 m) is only about half of the threshold we used for identifying a 'possible'

394 surging glacier.

395 In order to illustrate the impact of topography on the uncertainty, we calculated the NMAD of COP30 DEM – NASA DEM

396 difference over stable regions within different slope ranges (0-55°). As shown in Fig. 11, the uncertainties in elevation

397 difference observations increase as the terrain becomes steeper. Uncertainties over very steep regions (slope > 40°) can be two

398 times larger than over flat terrain (slope < 10°). Therefore, dH observations over crests, horns, and heads of glaciers, generally

399 have relatively large errors. In such regions, stereo optical images suffer from serious distortion, and sometimes have very low

400 brightness contrast due to snow cover; in the meantime, SAR images are affected by shadows and layover (Pieczonka and

401 Bolch, 2015). However, the terrain of main glacier bodies where surges usually occur is gentler, and therefore the uncertainties

of glacier surface elevation changes should be much lower than the thresholds that we used for identifying surges. Besides, the relatively large errors in dH maps are discontinuous in space, while the elevation changes used for identifying surges are spatially continuous. Hence, the uncertainty of glacier elevation change has no substantial impact on the identification of glacier surges.

Similar to previous studies (Sevestre and Benn, 2015; Goerlich et al., 2020), the surging glacier identification in this study was completed through a manual qualitative interpretation. It is difficult to provide a quantitative index to represent the uncertainty of surge identification. However, we have assigned a three-class indicator to represent the surge likelihood, which could aid that to a degree.

6.2 Characteristics of surging glaciers

The comparisons between geometric characteristics of surging and non-surging glaciers show that surge activity is more likely to occur in the glacier with a larger area, wider elevation range, and longer length (Figs. 7 and 8), which is consistent with previous studies (Barrand and Murray, 2006; Jiskoot, 2011; Sevestre and Benn, 2015; Mukherjee et al., 2017; Guillet et al., 2022).

Several studies have demonstrated that surging glaciers tend to have a shallower slope (Jiskoot et al., 2000; Guillet et al., 2022). However, we argue that this rule was concluded from an unbalanced comparison, as non-surging glaciers have a higher proportion of small glaciers than surging glaciers. Meanwhile, the inverse relationship between the glacier slope and length (Clarke, 1991; Sevestre and Benn, 2015) may not apply to very small glaciers (i.e. smaller than 1 km^2). As shown in Figs. 9d and 10, among the non-surging glaciers, the small ones occupy a high proportion and their mean slopes have strong variability. Thus, we can conclude that steeper glaciers are more likely to surge when the comparison is restricted to similar areas. As for the glacier median elevation, since it is almost uncorrelated to the glacier area, glacier length, glacier elevation range, and glacier mean slope (see Fig. 9), it can be deemed as an irregular glacier index. However, among glaciers that have similar areas, steeper glaciers generally have a lower median elevation. That's why the median elevation of surging glaciers is slightly smaller than that of non-surging glaciers (Fig. 8e).

These comparisons could now lead to a conclusion as follows: the surging glaciers are generally longer, and have a larger elevation range than non-surging glaciers, since they have more mass storage. However, when glaciers are similar in area, a steeper surface slope is more likely to lead to surge.

The spatial distribution of surging glaciers in HMA presents a strong heterogeneity. About 83% of identified surging glaciers are located in the northwestern region including the Central Tien Shan, Pamirs, Karakoram, and West Kunlun, and they occupy about 87% of the total identified surging glacier area (see Fig. 4 and Table 3). As discussed above, larger glaciers are more likely to surge. The northwest regions generally hold larger glaciers and therefore hold more surging glaciers. In other subregions, large glaciers are usually concentrated in some great ice fields, such as the Geladandong, Puruogangri, and Xinqingfeng. Surging glaciers in these subregions are usually clustered in a few watersheds.

6.3 Comparison with previous surging glacier inventories

Guillet et al. (2022) presented a comprehensive surging glacier inventory of HMA for the period 2000-2018 from a multi-factor remote sensing approach. Prior to the comparison, we generated an inventory based on the RGI6.0, as Guillet et al. (2022) did. Guillet et al. (2022) identified 666 surging glaciers, covering 19.5% of the total glacier area. We identified 890 surging glaciers (809 if represented by RGI6.0 polygons), covering 16.59% of the total glacier area. We attributed the lower area ratio of surging glaciers to two reasons. First, in our inventory, the surging tributaries were separated from the non-surging trunks. Second, many outcrop rocks and shaded areas are excluded from the GAMDAM2 glacier areas (Sakai, 2019), which would lower our surging area ratio, but make the result more accurate. If we assign our identified surging glaciers to the RGI6.0 polygons without tributary separation, the surging area ratio would be larger (20.25%).

443 Within our inventory, 556 surging and 62 surge-like glaciers were also identified by Guillet et al. (2022), and the discrepancy

444 of identifications mostly occurred on small glaciers. If only the period 2000-2020 was considered, 657 surging glaciers were

445 identified by us, which is very close to that of Guillet et al. (666). For the period 1970s-2000, we found 151 surging and 101

446 surge-like glaciers that were not identified by Guillet et al. (2022). Overall, we have newly identified 253 surging and 248

447 surge-like glaciers. We owed the new findings to the longer observation period and multiple elevation change observations.

448 However, 47 surging glaciers presented by Guillet et al. were missed in this study, and 62 surge-like glaciers in our new

449 inventory were identified as surging glaciers by Guillet et al. (2022). We checked the glaciers not included in our inventory

450 but included in the inventory of Guillet et al. (2022), as well as those included in our inventory but not included in Guillet et

451 al.'s inventory, and this step helped us to find 21 more surging glaciers. We attribute this to the missing criterion of flow

452 velocities, which could capture some small surges without obvious elevation change or morphological change. Besides, the

453 DEMs used in this study were suffering from data voids and incomplete spatial coverage, especially for the KH-9 DEM, which

454 could result in a relatively conservative identification.

455 Multiple studies have identified surging glaciers in the Karakoram based on different data sources. For example, Bhambri et

456 al. (2017) identified 221 surging and surge-like glaciers (counting tributaries of a glacier system as individual glaciers) based

457 on glacier morphological changes detected from space-borne optical images acquired from 1972 to 2016, in-situ observations,

458 and archive photos dating back to the 1840s. However, the boundary used by Bhambri et al. (2017) to define the extent of

459 Karakoram is much smaller than that used in our inventory. A much smaller group of surging glaciers (88) was identified by

460 Copland et al. (2011) based on a similar method and the data acquired between 1960 and 2013. Rankl et al. (2014) identified

461 101 surging glaciers in the Karakoram by detecting changes in glacier surface velocity and terminus position between 1976

462 and 2012. The results of Guillet et al. (2022) should be more reliable than previous ones because more criteria were used for

463 identifying surging glaciers. Compared with previous inventories, our inventory includes more surging glaciers in the

464 Karakoram (354). Among the 223 surging glaciers in the Karakoram identified by Guillet et al. (2022), 203 were identified as

465 surging glaciers, and 12 were identified as surge-like glaciers in this study, which means only 8 surging glaciers presented by

466 Guillet et al. (2022) were not included in our inventory. The high coincidence between the two inventories indicates our surging

467 glacier identification result is reliable. In total, we have newly identified 101 surging and 101 surge-like glaciers in this region.

468 Based on the method of glacier terminus change monitoring in Google Earth Engine, Vale et al. (2021) identified changes in

469 the terminus of 137 surging glaciers. In total, 127 verified surging and 6 surge-like glaciers in our inventory were included in

470 their inventory, i.e., only four glaciers were missed in this study. We found these four missing surging glaciers had slight

471 terminus advancing (<200 m) during long surging periods (>10 years). The very slow and slight terminus advance is difficult

472 to identify through visual interpretation.

473 In the Pamirs, Sevestre and Benn (2015) identified 820 surge-type glaciers based on publications and reports, but Goerlich et

474 al. (2020) reported only 186 surging glaciers based on observations of glacier flow velocity, elevation change, etc. We found

475 that if Goerlich et al. (2020) applied the GAMDAM2 glacier polygons used in this study, the number of identified surging

476 glaciers would be 182. Among the 182 surging glaciers identified by Goerlich et al. (2020), 153 were identified as surging

477 glaciers and 15 were identified as surge-like glaciers in our study. Although 14 surging glaciers are missed in this study, our

478 inventory contains another 94 surging and 44 surge-like glaciers. The main cause for the discrepancy is that the glacier

479 elevation change observations before 2000 used by Goerlich et al. (2020) only cover a small part of the Western Pamir. In this

480 region, our inventory shared 193 surging glaciers with Guillet et al.'s inventory, and 185 of them were identified during the

481 period 2000-2020, which also manifests a high coincidence of the two results.

482 In the West Kunlun, Yasuda and Furuya (2015) reported 9 surging glaciers in the main range only, based on changes in glacier

483 flow velocity and terminus position of 31 glaciers, and another 9 surging glaciers were found in the northwest part of the West

484 Kunlun Shan by Chudley et al. (2019). A larger number (60) were found by Guillet et al. (2022). However, our inventory

485 includes even more surging (82) and surge-like (47) glaciers in the West Kunlun Shan. For the period 2000-2020, we identified

61 surging glaciers, which is very close to the number presented by Guillet et al. (2022). In Central Tien Shan, Mukherjee et al. (2017) identified 39 surge-type (including 9 surging and 13 very probable surging) glaciers through the analysis of changes in surface elevation and morphology from 1964 to 2014, whereas 79 (59 surging and 20 surge-like) were identified in our study. The insufficient coverage of elevation change observation (only covering the west part of the Central Tien Shan) may be the main reason for the discrepancy in identification results. Guillet et al. (2022) identified 54 surging glaciers during 2000-2018, from which 36 were confirmed in our inventory.

7 Conclusions

This study presents a new inventory of surging glaciers across the entire HMA range. For the surge identification, we relied on glacier surface elevation changes derived from multiple elevation sources, and complementarily on optical satellite images for assessing morphological changes. In total, 890 surging and 336 probably or possibly surging glaciers were identified in the new inventory. Through the analysis of geometric parameters, we found that surging glaciers generally have a greater area, length, and elevation range than non-surging glaciers. However, the differences are smaller when taking the glacier size distribution into account. When considering glaciers of similar areas, the steeper ones are more likely to surge. Benefiting from the long period and wide coverage of surface elevation change observations, our study newly identified 253 surging and 248 surge-like glaciers in HMA compared to the previous inventory (Guillet et al., 2022). However, our inventory does not provide the surge duration period and the maximum flow velocity, which are useful to describe the dynamic process of each glacier surge activity. Improvements should be made by combining multi-criteria identification methods. Considering the fact that glacier surges are more widespread than we thought, the inventory presented in this study still needs further improvement.

8 Data and code availability

The presented inventory and the multi-temporal elevation change results used to identify surging glaciers are freely available at: https://doi.org/10.5281/zenodo.7961207 (Guo et al., 2022). The inventory contains glacier outlines and manually defined center points of surging glaciers with geometric attributes and is distributed in GeoPackage (.gpkg) and ESRI shapefile (.shp) formats. The glacier polygons are compiled from the GAMDAM2 glacier inventory. In total, eight fields are integrated into the attributes table to describe the surging information of the corresponding glacier as mentioned in section 5.3. The description of each field in the attribute table is listed in Table 5. The DEM differences (COP30 DEM – NASA DEM, HMA DEM – NASA DEM, and NASA DEM – KH-9 DEM) are compressed into individual zip files, respectively. The elevation change results of surging glaciers were divided into multi-temporal 1° × 1° tiled GeoTiff grids. The metadata file is stored in a text file (README.txt), which contains the datasets description and details of the attribute information of the inventory.

The code used for elevation change estimation is available at: https://github.com/TristanBlus/dem_coreg. This code was developed based on the *demcoreg* package (Shean et al., 2019).

Author contribution

J.L. and L.G. conceived this study and wrote the paper. L.G. developed the processing flow, complied the inventory, and drew the figures with support from J.L. A.D. generated the KH-9 DEM. A.D., Z.L., and X.L. helped with the results analysis and discussions, as well as manuscript editing. Z.L., J.L., and J.Z. provided funding acquisition. All authors have contributed and agreed to the published version of the manuscript.

References

Abdel Jaber, W., Rott, H., Floricioiu, D., Wuite, J., and Miranda, N.: Heterogeneous spatial and temporal pattern of surface elevation change and mass balance of the Patagonian ice fields between 2000 and 2016, The Cryosphere, 13, 2511–2535, doi:10.5194/tc-13-2511-2019, 2019.

AIRBUS: Copernicus Digital Elevation Model Validation Report, AIRBUS Defence and Space GmbH, 2020.

Barrand, N. E. and Murray, T.: Multivariate Controls on the Incidence of Glacier Surging in the Karakoram Himalaya, Arct. Antarct. Alp. Res., 38, 489–498, doi:10.1657/1523-0430(2006)38[489:MCOTIO]2.0.CO;2, 2006.

Beaud, F., Aati, S., Delaney, I., Adhikari, S., and Avouac, J.-P.: Generalized sliding law applied to the surge dynamics of Shisper Glacier and constrained by timeseries correlation of optical satellite images, Glaciers/Remote Sensing, doi:10.5194/tc-2021-96, 2021.

Benn, D. I., Fowler, A. C., Hewitt, I., and Sevestre, H.: A general theory of glacier surges, J. Glaciol., 65, 701–716, doi:10.1017/jog.2019.62, 2019.

Bhambri, R., Hewitt, K., Kawishwar, P., and Pratap, B.: Surge-type and surge-modified glaciers in the Karakoram, Sci. Rep., 7, doi:10.1038/s41598-017-15473-8, 2017.

Bhambri, R., Hewitt, K., Haritashya, U. K., Chand, P., Kumar, A., Verma, A., Tiwari, S. K., and Rai, S. K.: Characteristics of surge-type tributary glaciers, Karakoram, Geomorphology, 403, 108161, doi:10.1016/j.geomorph.2022.108161, 2022.

Bolch, T., Kulkarni, A., Kaab, A., Huggel, C., Paul, F., Cogley, J. G., Frey, H., Kargel, J. S., Fujita, K., Scheel, M., Bajracharya, S., and Stoffel, M.: The State and Fate of Himalayan Glaciers, Science, 336, 310–314, doi:10.1126/science.1215828, 2012.

Bolch, T., Pieczonka, T., Mukherjee, K., and Shea, J.: Brief communication: Glaciers in the Hunza catchment (Karakoram) have been nearly in balance since the 1970s, The Cryosphere, 11, 531–539, doi:10.5194/tc-11-531-2017, 2017.

Bolch, T., Shea, J. M., Liu, S., Azam, F. M., Gao, Y., Gruber, S., Immerzeel, W. W., Kulkarni, A., Li, H., Tahir, A. A., Zhang, G., and Zhang, Y.: Status and Change of the Cryosphere in the Extended Hindu Kush Himalaya Region, in: The Hindu Kush

Himalaya Assessment, edited by: Wester, P., Mishra, A., Mukherji, A., and Shrestha, A. B., Springer International Publishing, Cham, 209–255, doi:10.1007/978-3-319-92288-1_7, 2019.

Brun, F., Berthier, E., Wagnon, P., Kääb, A., and Treichler, D.: A spatially resolved estimate of High Mountain Asia glacier mass balances from 2000 to 2016, Nat. Geosci., 10, 668–673, doi:10.1038/ngeo2999, 2017.

Chudley, T. R. and Willis, I. C.: Glacier surges in the north-west West Kunlun Shan inferred from 1972 to 2017 Landsat imagery, J. Glaciol., 65, 1–12, doi:10.1017/jog.2018.94, 2019.

Clarke, G. K. C.: Length, width and slope influences on glacier surging, J. Glaciol., 37, 236–246, doi:10.3189/S0022143000007255, 1991.

Clarke, G. K. C., Schmok, J. P., Ommanney, C. S. L., and Collins, S. G.: Characteristics of surge-type glaciers, J. Geophys. Res. Solid Earth, 91, 7165–7180, doi:10.1029/JB091iB07p07165, 1986.

Cogley, J. G., Arendt, A. A., Bauder, A., Braithwaite, R. J., Hock, R., J, B., R., Jansson, P., Kaser, G., Moller, M., Nicholson, L., Rasmussen, L. A., and Zemp, M.: Glossary of glacier mass balance and related terms, IACS Contribution No.2, UNESCO, Paris, 2011.

Copland, L., Sylvestre, T., Bishop, M. P., Shroder, J. F., Seong, Y. B., Owen, L. A., Bush, A., and Kamp, U.: Expanded and Recently Increased Glacier Surging in the Karakoram, Arct. Antarct. Alp. Res., 43, 503–516, 2011.

Crippen, R., Buckley, S., Agram, P., Belz, E., Gurrola, E., Hensley, S., Kobrick, M., Lavalle, M., Martin, J., Neumann, M., Nguyen, Q., Rosen, P., Shimada, J., Simard, M., and Tung, W.: NASADEM global elevation model: methods and progress, ISPRS - Int. Arch. Photogramm. Remote Sens. Spat. Inf. Sci., XLI-B4, 125–128, doi:10.5194/isprsarchives-XLI-B4-125-2016, 2016.

Dehecq, A., Gardner, A. S., Alexandrov, O., McMichael, S., Hugonnet, R., Shean, D., and Marty, M.: Automated Processing of Declassified KH-9 Hexagon Satellite Images for Global Elevation Change Analysis Since the 1970s, Front. Earth Sci., 8, 566802, doi:10.3389/feart.2020.566802, 2020.

Fan, Y., Ke, C.-Q., Zhou, X., Shen, X., Yu, X., and Lhakpa, D.: Glacier mass-balance estimates over High Mountain Asia from 2000 to 2021 based on ICESat-2 and NASADEM, J. Glaciol., 1–13, doi:10.1017/jog.2022.78, 2022.

Farinotti, D., Immerzeel, W. W., Kok, R., Quincey, D. J., and Dehecq, A.: Manifestations and mechanisms of the Karakoram glacier Anomaly, Nat. Geosci., 13, 8–16, doi:10.1038/s41561-019-0513-5, 2020.

Farnsworth, W. R., Ingólfsson, Ó., Retelle, M., and Schomacker, A.: Over 400 previously undocumented Svalbard surge-type glaciers identified, Geomorphology, 264, 52–60, doi:10.1016/j.geomorph.2016.03.025, 2016.

Farr, T. G., Rosen, P. A., Caro, E., Crippen, R., Duren, R., Hensley, S., Kobrick, M., Paller, M., Rodriguez, E., Roth, L., Seal, D., Shaffer, S., Shimada, J., Umland, J., Werner, M., Oskin, M., Burbank, D., and Alsdorf, D.: The Shuttle Radar Topography Mission, Rev. Geophys., 45, RG2004, doi:10.1029/2005RG000183, 2007.

Fowler, A. C.: A theory of glacier surges, J. Geophys. Res., 92, 9111, doi:10.1029/JB092iB09p09111, 1987.

Fowler, A. C., Murray, T., and Ng, F. S. L.: Thermally controlled glacier surging, J. Glaciol., 47, 527–538, doi:10.3189/172756501781831792, 2001.

Gardelle, J., Berthier, E., Arnaud, Y., and Kääb, A.: Region-wide glacier mass balances over the Pamir-Karakoram-Himalaya during 1999–2011, Cryosphere Discuss., 7, 975–1028, doi:10.5194/tcd-7-975-2013, 2013.

Goerlich, F., Bolch, T., and Paul, F.: More dynamic than expected: an updated survey of surging glaciers in the Pamir, Earth Syst. Sci. Data, 12, 3161–3176, doi:10.5194/essd-12-3161-2020, 2020.

Guillet, G., King, O., Lv, M., Ghuffar, S., Benn, D., Quincey, D., and Bolch, T.: A regionally resolved inventory of High Mountain Asia surge-type glaciers, derived from a multi-factor remote sensing approach, The Cryosphere, 16, 603–623, doi:10.5194/tc-16-603-2022, 2022.

Guth, P. L. and Geoffroy, T. M.: LiDAR point cloud and ICESat-2 evaluation of 1 second global digital elevation models: Copernicus wins, Trans. GIS, 25, 2245–2261, doi:10.1111/tgis.12825, 2021.

Hewitt, K.: The Karakoram Anomaly? Glacier Expansion and the 'Elevation Effect,' Karakoram Himalaya, Mt. Res. Dev., 25, 332–340, doi:10.1659/0276-4741(2005)025[0332:TKAGEA]2.0.CO;2, 2005.

Hewitt, K.: Tributary glacier surges: an exceptional concentration at Panmah Glacier, Karakoram Himalaya, J. Glaciol., 53, 181–188, doi:10.3189/172756507782202829, 2007.

Höhle, J. and Höhle, M.: Accuracy assessment of digital elevation models by means of robust statistical methods, ISPRS J. Photogramm. Remote Sens., 64, 398–406, doi:10.1016/j.isprsjprs.2009.02.003, 2009.

Holzer, N., Vijay, S., Yao, T., Xu, B., Buchroithner, M., and Bolch, T.: Four decades of glacier variations at Muztagh Ata (eastern Pamir): a multi-sensor study including Hexagon KH-9 and Pléiades data, The Cryosphere, 9, 2071–2088, doi:10.5194/tc-9-2071-2015, 2015.

Hugonnet, R., McNabb, R., Berthier, E., Menounos, B., Nuth, C., Girod, L., Farinotti, D., Huss, M., Dussaillant, I., Brun, F., and Kääb, A.: Accelerated global glacier mass loss in the early twenty-first century, Nature, 592, 726–731, doi:10.1038/s41586-021-03436-z, 2021.

Jacquemart, M. and Cicoira, A.: Hazardous Glacier Instabilities: Ice Avalanches, Sudden Large-Volume Detachments of Low-Angle Mountain Glaciers, and Glacier Surges, in: Treatise on Geomorphology, Elsevier, 330–345, doi:10.1016/B978-0-12-818234-5.00188-7, 2022.

Jiskoot, H.: Glacier Surging, in: Encyclopedia of Snow, Ice and Glaciers, edited by: Singh, V. P., Singh, P., and Haritashya, U. K., Springer Netherlands, Dordrecht, 415–428, doi:10.1007/978-90-481-2642-2_559, 2011.

Jiskoot, H., Murray, T., and Boyle, P.: Controls on the distribution of surge-type glaciers in Svalbard, J. Glaciol., 46, 412–422, doi:10.3189/172756500781833115, 2000.

Kamb, B.: Glacier surge mechanism based on linked cavity configuration of the basal water conduit system, J. Geophys. Res., 92, 9083, doi:10.1029/JB092iB09p09083, 1987.

Leclercq, P. W., Kääb, A., and Altena, B.: Brief communication: Detection of glacier surge activity using cloud computing of Sentinel-1 radar data, The Cryosphere, 15, 4901–4907, doi:10.5194/tc-15-4901-2021, 2021.

Li, J., Li, Z., Zhu, J., Li, X., Xu, B., Wang, Q., Huang, C., and Hu, J.: Early 21st century glacier thickness changes in the Central Tien Shan, Remote Sens. Environ., 192, 12–29, doi:10.1016/j.rse.2017.02.003, 2017.

Lv, M., Guo, H., Lu, X., Liu, G., Yan, S., Ruan, Z., Ding, Y., and Quincey, D. J.: Characterizing the behaviour of surge- and non-surge-type glaciers in the Kingata Mountains, eastern Pamir, from 1999 to 2016, The Cryosphere, 13, 219–236, doi:10.5194/tc-13-219-2019, 2019.

Lv, M., Guo, H., Yan, J., Wu, K., Liu, G., Lu, X., Ruan, Z., and Yan, S.: Distinguishing Glaciers between Surging and Advancing by Remote Sensing: A Case Study in the Eastern Karakoram, Remote Sens., 12, 2297, doi:10.3390/rs12142297, 2020.

Maurer, J. M., Schaefer, J. M., Rupper, S., and Corley, A.: Acceleration of ice loss across the Himalayas over the past 40 years, Sci. Adv., 5, eaav7266, doi:10.1126/sciadv.aav7266, 2019.

Maussion, F., Scherer, D., Mölg, T., Collier, E., Curio, J., and Finkelnburg, R.: Precipitation Seasonality and Variability over the Tibetan Plateau as Resolved by the High Asia Reanalysis, J. Clim., 27, 1910–1927, doi:10.1175/JCLI-D-13-00282.1, 2014.

Maussion, F., Butenko, A., Champollion, N., Dusch, M., Eis, J., Fourteau, K., Gregor, P., Jarosch, A. H., Landmann, J., Oesterle, F., Recinos, B., Rothenpieler, T., Vlug, A., Wild, C. T., and Marzeion, B.: The Open Global Glacier Model (OGGM) v1.1, Geosci. Model Dev., 12, 909–931, doi:10.5194/gmd-12-909-2019, 2019.

Mukherjee, K., Bolch, T., Goerlich, F., Kutuzov, S., Osmonov, A., Pieczonka, T., and Shesterova, I.: Surge-Type Glaciers in the Tien Shan (Central Asia), Arct. Antarct. Alp. Res., 49, 147–171, doi:10.1657/AAAR0016-021, 2017.

Murray, T., Strozzi, T., Luckman, A., Jiskoot, H., and Christakos, P.: Is there a single surge mechanism? Contrasts in dynamics between glacier surges in Svalbard and other regions: IS THERE A SINGLE SURGE MECHANISM?, J. Geophys. Res. Solid Earth, 108, doi:10.1029/2002JB001906, 2003.

643 Nuimura, T., Sakai, A., Taniguchi, K., Nagai, H., Lamsal, D., Tsutaki, S., Kozawa, A., Hoshina, Y., Takenaka, S., Omiya, S.,

644 Tsunematsu, K., Tshering, P., and Fujita, K.: The GAMDAM glacier inventory: a quality-controlled inventory of Asian

645 glaciers, The Cryosphere, 9, 849–864, doi:10.5194/tc-9-849-2015, 2015.

646 Nuth, C. and Kääb, A.: Co-registration and bias corrections of satellite elevation data sets for quantifying glacier thickness

647 change, The Cryosphere, 5, 271–290, doi:10.5194/tc-5-271-2011, 2011.

648 Paul, F.: Revealing glacier flow and surge dynamics from animated satellite image sequences: examples from the Karakoram,

649 The Cryosphere, 9, 2201–2214, doi:10.5194/tc-9-2201-2015, 2015.

650 Pieczonka, T. and Bolch, T.: Region-wide glacier mass budgets and area changes for the Central Tien Shan between ~1975

651 and 1999 using Hexagon KH-9 imagery, Glob. Planet. Change, 128, 1–13, doi:10.1016/j.gloplacha.2014.11.014, 2015.

652 Purinton, B. and Bookhagen, B.: Beyond Vertical Point Accuracy: Assessing Inter-pixel Consistency in 30 m Global DEMs

653 for the Arid Central Andes, Front. Earth Sci., 9, 758606, doi:10.3389/feart.2021.758606, 2021.

654 Quincey, D. J., Braun, M., Glasser, N. F., Bishop, M. P., Hewitt, K., and Luckman, A.: Karakoram glacier surge dynamics,

655 Geophys. Res. Lett., 38, L18504, doi:10.1029/2011GL049004, 2011.

656 Rankl, M., Kienholz, C., and Braun, M.: Glacier changes in the Karakoram region mapped by multimission satellite imagery,

657 The Cryosphere, 8, 977–989, doi:10.5194/tc-8-977-2014, 2014.

658 Rott, H., Sturm, K., and Miller, H.: Active and passive microwave signatures of Antarctic firn by means of field measurements

659 and satellite data, Ann. Glaciol., 17, 337–343, doi:10.3189/S0260305500013070, 1993.

660 Round, V., Leinss, S., Huss, M., Haemmig, C., and Hajnsek, I.: Surge dynamics and lake outbursts of Kyagar Glacier,

661 Karakoram, The Cryosphere, 11, 723–739, doi:10.5194/tc-11-723-2017, 2017.

662 Sakai, A.: Brief communication: Updated GAMDAM glacier inventory over high-mountain Asia, The Cryosphere, 13, 2043–

663 2049, doi:10.5194/tc-13-2043-2019, 2019.

664 Sevestre, H. and Benn, D. I.: Climatic and geometric controls on the global distribution of surge-type glaciers: implications

665 for a unifying model of surging, J. Glaciol., 61, 646–662, doi:10.3189/2015JoG14J136, 2015.

666 Shean, D., Shashank Bhushan, Lilien, D., and Meyer, J.: dshean/demcoreg: Zenodo DOI release, ,

667 doi:10.5281/ZENODO.3243481, 2019.

668 Shean, D. E., Alexandrov, O., Moratto, Z. M., Smith, B. E., Joughin, I. R., Porter, C., and Morin, P.: An automated, open-

669 source pipeline for mass production of digital elevation models (DEMs) from very-high-resolution commercial stereo satellite

670 imagery, ISPRS J. Photogramm. Remote Sens., 116, 101–117, doi:10.1016/j.isprsjprs.2016.03.012, 2016.

671 Shean, D. E., Bhushan, S., Montesano, P., Rounce, D. R., Arendt, A., and Osmanoglu, B.: A Systematic, Regional Assessment

672 of High Mountain Asia Glacier Mass Balance, Front. Earth Sci., 7, 363, doi:10.3389/feart.2019.00363, 2020.

673 Surazakov, A. and Aizen, V.: Positional Accuracy Evaluation of Declassified Hexagon KH-9 Mapping Camera Imagery,

674 Photogramm. Eng. Remote Sens., 76, 603–608, doi:10.14358/PERS.76.5.603, 2010.

675 Thøgersen, K., Gilbert, A., Schuler, T. V., and Malthe-Sørenssen, A.: Rate-and-state friction explains glacier surge propagation,

676 Nat. Commun., 10, 2823, doi:10.1038/s41467-019-10506-4, 2019.

677 Vale, A. B., Arnold, N. S., Rees, W. G., and Lea, J. M.: Remote Detection of Surge-Related Glacier Terminus Change across

678 High Mountain Asia, Remote Sens., 13, 1309, doi:10.3390/rs13071309, 2021.

679 Van Wyk de Vries, M., Wickert, A. D., MacGregor, K. R., Rada, C., and Willis, M. J.: Atypical landslide induces speedup,

680 advance, and long-term slowdown of a tidewater glacier, Geology, doi:10.1130/G49854.1, 2022.

681 Yamazaki, D., Ikeshima, D., Tawatari, R., Yamaguchi, T., O'Loughlin, F., Neal, J. C., Sampson, C. C., Kanae, S., and Bates,

682 P. D.: A high-accuracy map of global terrain elevations, Geophys. Res. Lett., 44, 5844–5853, doi:10.1002/2017GL072874,

683 2017.

684 Yasuda, T. and Furuya, M.: Dynamics of surge-type glaciers in West Kunlun Shan, Northwestern Tibet, J. Geophys. Res.

685 Earth Surf., 120, 2393–2405, doi:10.1002/2015JF003511, 2015.

686 Zhou, S., Yao, X., Zhang, D., Zhang, Y., Liu, S., and Min, Y.: Remote Sensing Monitoring of Advancing and Surging Glaciers

687 in the Tien Shan, 1990–2019, Remote Sens., 13, 1973, doi:10.3390/rs13101973, 2021.

688 Zhou, Y., Li, Z., and Li, J.: Slight glacier mass loss in the Karakoram region during the 1970s to 2000 revealed by KH-9

689 images and SRTM DEM, J. Glaciol., 63, 331–342, doi:10.1017/jog.2016.142, 2017.

690 Zhou, Y., Li, Z., Li, J., Zhao, R., and Ding, X.: Glacier mass balance in the Qinghai–Tibet Plateau and its surroundings from

691 the mid-1970s to 2000 based on Hexagon KH-9 and SRTM DEMs, Remote Sens. Environ., 210, 96–112,

692 doi:10.1016/j.rse.2018.03.020, 2018.

693 **Tables and Figures**

694 **Table 1: Criteria for identifying surging glaciers based on changes in elevation and morphological features.**

Surging feature	Identified class	Description
Elevation change	I-a	obvious thickening in lower reaches (e.g., ±30m)
	I-b	contrasting upper-thinning and lower-thickening (e.g., ±20m)
	I-c	contrasting upper-thickening and lower-thinning (e.g., +20m and -30m)
	I-d	severe thinning in the lower reaches (e.g., two times stronger than normal glaciers)
	II-e	moderate upper thinning and lower thickening (e.g., ±15m)
	II-f	only moderate thickening in the middle reaches (e.g., +15m)
	III-g	only moderate thickening at the terminus (e.g., +15m)
	III-h	only strong thinning in the lower reaches (e.g., one time stronger than normal glaciers)
Terminus advance	T1	strong terminus advancing (e.g., >500m)
	T2	slight terminus advancing (e.g., 0~500m)
Moraine change	M1	fast change of the looped moraine, or obvious distortion of the medial moraine
	M2	slow shape change of the looped moraine, or slight distortion of the medial moraine

695

696 **Table 2: Surging glacier identification results.**

Glacier changes	Identification class			Total
	I/T1/M1	II/T2/M2	III	
2000-2020 elevation change	719	157	169	1045
1970s-2000 elevation change	507	156	57	720
1986-2021 terminus advance	247	397	-	645
1986-2021 looped moraine	112	31	-	144
1986-2021 medial moraine	69	29	-	108
Final identified surging glaciers	890 (verified)	208 (probable)	128 (possible)	1226

697

698 **Table 3: Results of surging glacier identification in 22 subregions of HMA. Only glaciers larger than 0.4 km² were considered in the**
699 **glacier number related values.**

HiMAP regions	Glacier Number				Glacier Area (km²)			
	Surging	Surge-like	Total	Ratio* (%)	Surging	Surge-like	Total	Ratio* (%)
Karakoram	354	128	4121	8.59	7936.12	1329.40	20103.68	39.48
Western Pamir	188	48	3058	6.15	2232.52	289.597	8172.64	27.32
Western Kunlun Shan	82	47	2508	3.27	2580.21	589.17	8466.12	30.48
Central Tien Shan	59	20	2248	2.62	881.61	305.47	6816.95	12.93

Eastern Pamir	56	16	1148	4.88	796.35	79.12	2746.47	29.00
Tanggula Shan	22	4	697	3.16	441.94	41.71	1937.39	22.81
Tibetan Interior Mountains	22	12	1471	1.50	286.29	140.22	3933.48	7.28
Northern Western Tien Shan	21	6	1374	1.53	116.27	81.09	2502.60	4.65
Central Himalaya	17	21	3433	0.50	164.12	185.07	9928.72	1.65
Eastern Kunlun Shan	16	7	1191	1.34	458.11	55.38	2960.26	15.48
Nyainqentanglha	10	5	2916	0.34	119.53	184.79	7216.62	1.66
Eastern Hindu Kush	9	5	1279	0.70	178.18	77.19	3055.80	5.83
Western Himalaya	9	4	3659	0.25	110.22	69.41	8619.19	1.28
Eastern Himalaya	6	0	1334	0.45	94	0	3371.89	2.79
Pamir Alay	5	0	991	0.50	35.72	0	1957.94	1.82
Qilian Shan	4	6	851	0.47	35.99	26.40	1627.94	2.21
Eastern Tibetan Mountains	3	2	156	1.92	36.33	3.85	341.46	10.64
Altun Shan	2	3	156	1.28	4.13	3.17	294.95	1.40
Eastern Tien Shan	2	1	1243	0.16	12.03	2.59	2440.11	0.49
Hengduan Shan	2	0	700	0.29	26.22	0	1335.39	1.96
Gangdise Mountains	1	0	768	0.13	10.52	0	1339.54	0.79
Dzhungarsky Alatau	0	1	407	0	0	10.98	648.61	0
Total	890	336	35709	2.49	16556.42	3474.60	99817.72	16.59

700   * The value of ratio only considered the number and area of verified surging glaciers.

701

702   **Table 4: The number and area ratios of surging glaciers in all glaciers for different area classes.**

Area Class	Total		Surging Glacier		Ratio (%)	
	Count	Area (km^2)	Count	Area (km^2)	Count	Area
0.4-1	19428	12215.4	28	20.8	0.14	0.17
1-3	10983	18305.7	169	345.0	1.54	1.88
3-5	2404	9229.4	141	560.3	5.87	6.07
5-10	1650	11370.1	195	1416.4	11.82	12.46
10-30	946	15048.9	227	3861.2	24.00	25.66
30-50	161	5979.1	56	2036.5	34.78	34.06
50-100	92	6337.4	48	3329.2	52.17	52.53
100-300	39	6191.4	24	3651.5	61.54	58.98
>300	6	3466.3	2	1335.6	33.33	38.53

703

704   **Table 5: Attribute information in the present surging glacier inventory.**

| Attribute	Description	Attribute	Description
Glac_ID	Glacier identifier composed by Lat/Lon	Surge_20	Surge identified in 2000-2020 by dH
Area	Glacier area (km^2)	Surge_70s	Surge identified in 1970s-2000 by dH
Zmin	Minimum elevation of the glacier (m a.s.l)	Delta_T	Identified class of glacier terminus advance
Zmax	Maximum elevation of the glacier (m a.s.l)	Loop_M	Identified class of looped moraine change
Zmed	Median elevation of the glacier (m a.s.l)	Medial_M	Identified class of medial moraine change
Slope	Mean glacier surface slope (°)	False_signal	False positive signal of identification
Aspect	Mean glacier aspect/orientation (°)	Trib_surge	If the glacier has/is surging tributary
MaxL	Maximum length of glacier flow line (m)	Surge_class	Final surge identification during 1970s-2020
HiMAP_region	HMA subregion that the glacier belongs to		

705

19
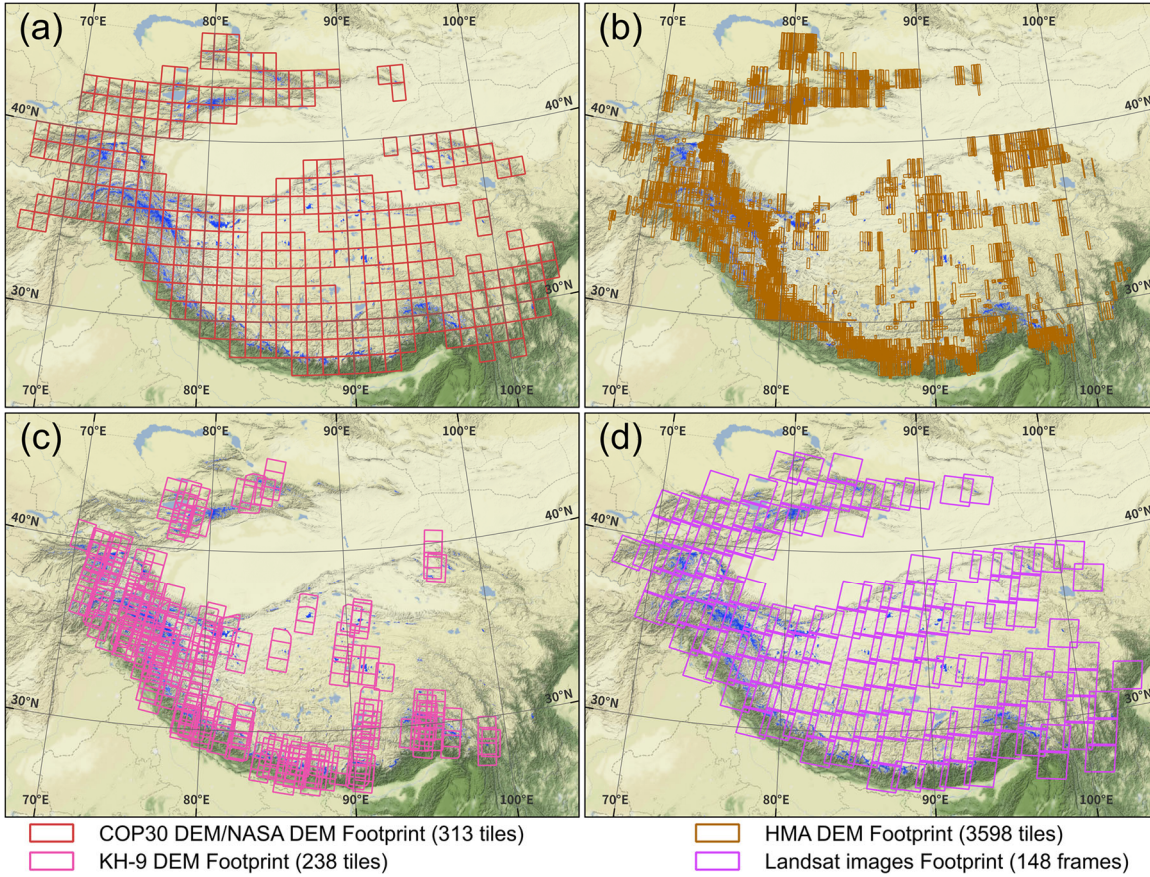
Figure 1: Footprints of (a) the COP30/NASA DEMs, (b) the HMA DEMs, (c) the KH-9 DEMs, and (d) Landsat imageries that were used in this study. The background is rendered from the ESRI World Physical base map (Source: US National Park Service).
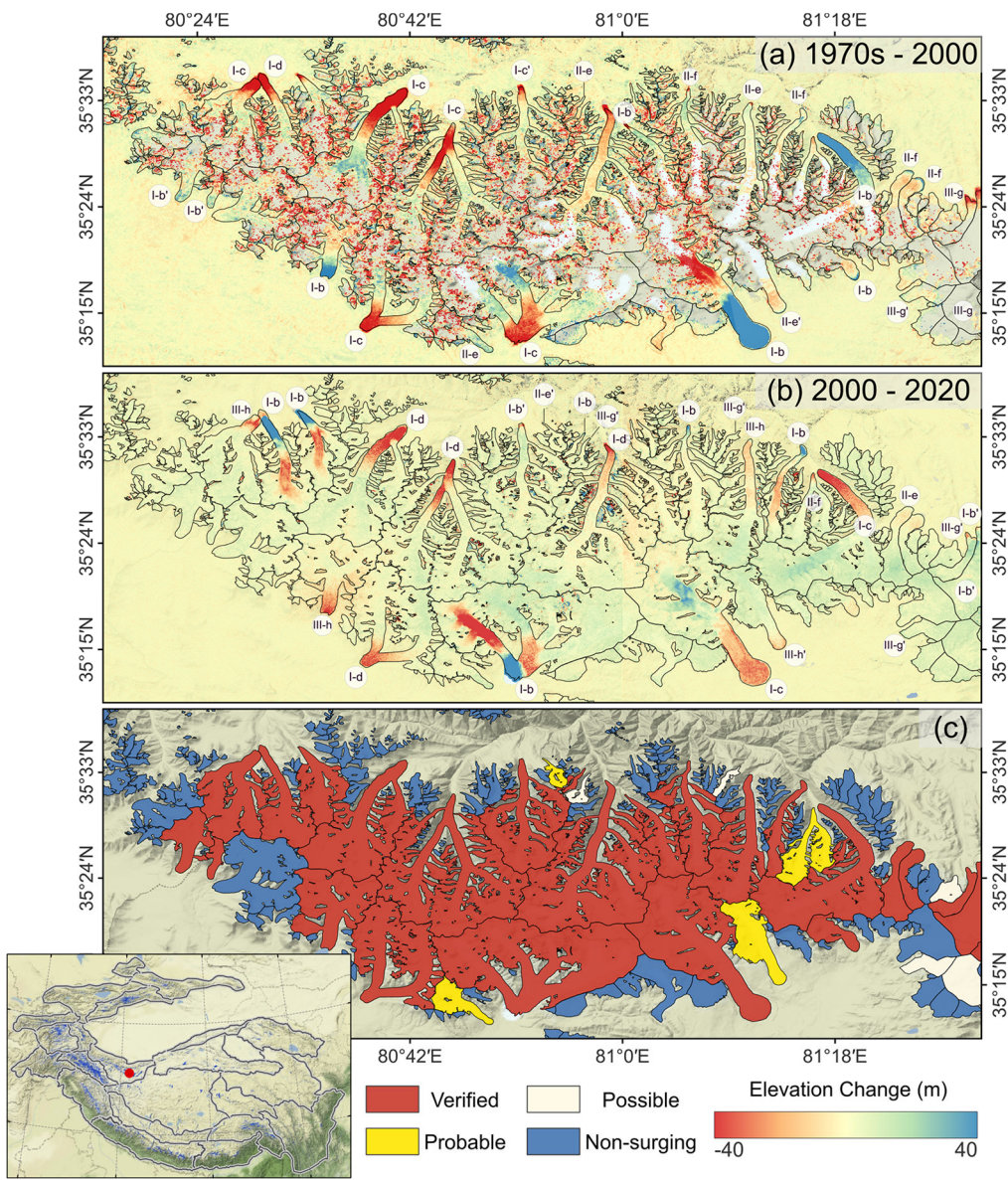
Figure 2: An example of derived elevation change maps during (a) 1970s-2000, (b) 2000-2020, and (c) the surging glacier identification results. Black curves are glacier outlines. The labels in panels (a) and (b) represent the identified classes based on the elevation change patterns (the criteria of identification are elaborated in section 4.2.1 and Table 1). The subscript '′' in the labels indicates that the surging glacier is identified by combining other elevation change maps. The red circle in the inset panel denotes the location of the area in the main panel (Western Kunlun Shan). The background is the shaded relief of the COP30 DEM (Source: ESA).
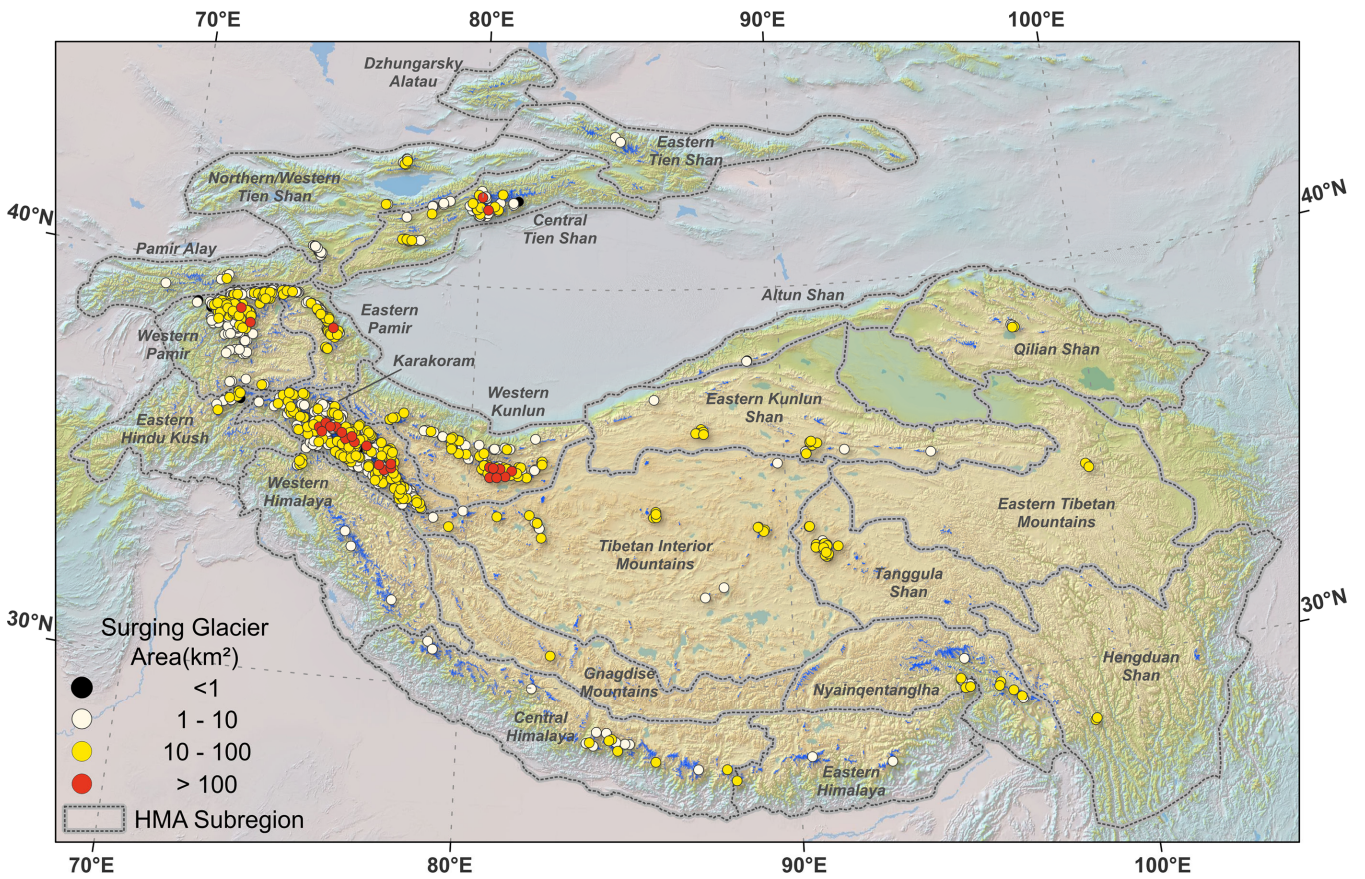
Figure 3: Overview of the distribution of identified surging glaciers in 22 subregions of HMA. The background is the shaded relief of SRTM DEM (Source: USGS).
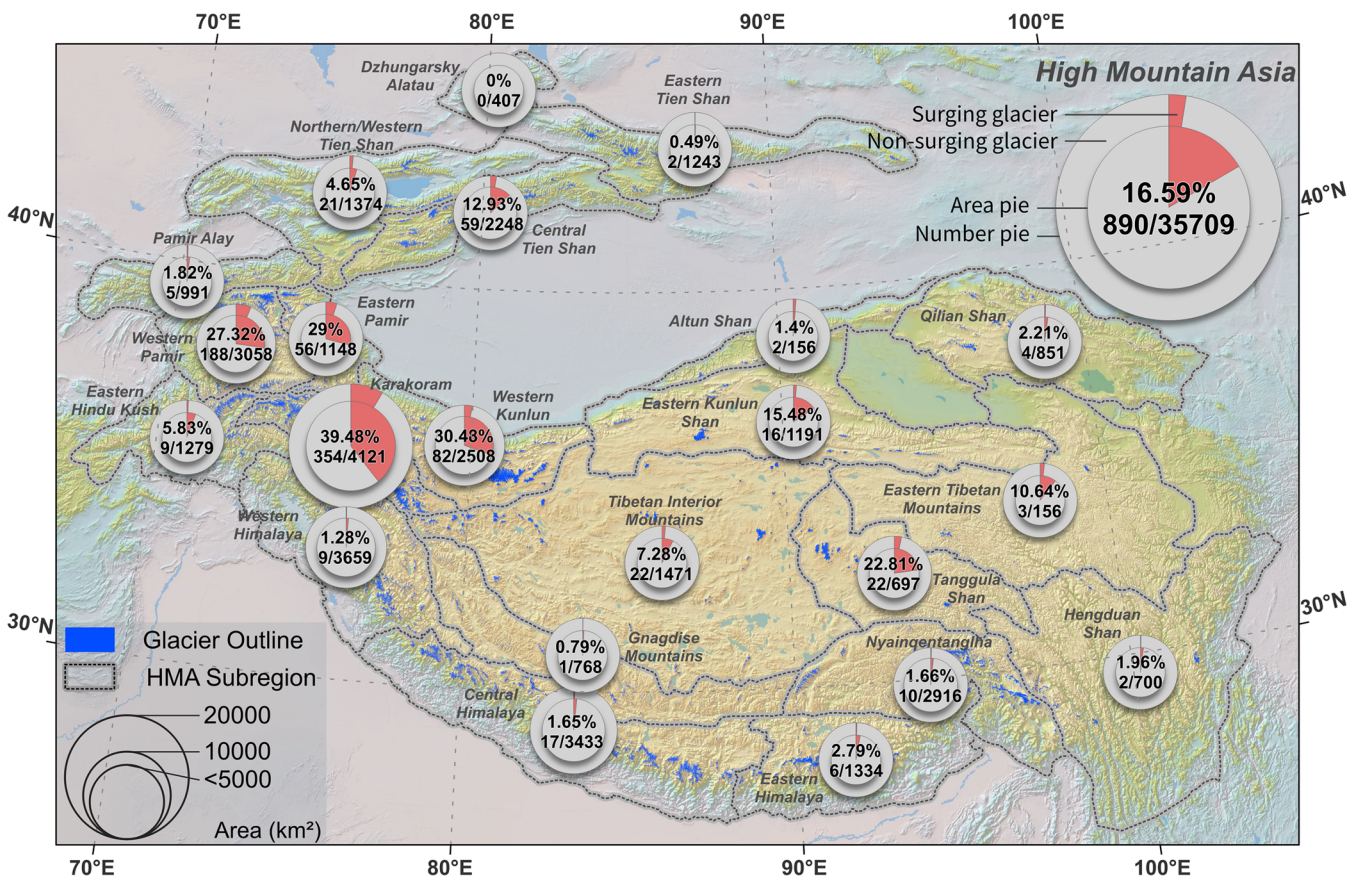
Figure 4: Distribution of surging glaciers in the 22 subregions of HMA. The double-level pie chart represents the ratios of surging glacier number and area in each subregion. The inner pie denotes the area ratio labeled by a percentage, and the outer pie denotes

the number ratio labeled by a fraction (only glaciers larger than 0.4 km^2 are considered). The background is the shaded relief of
SRTM DEM (Source: USGS).
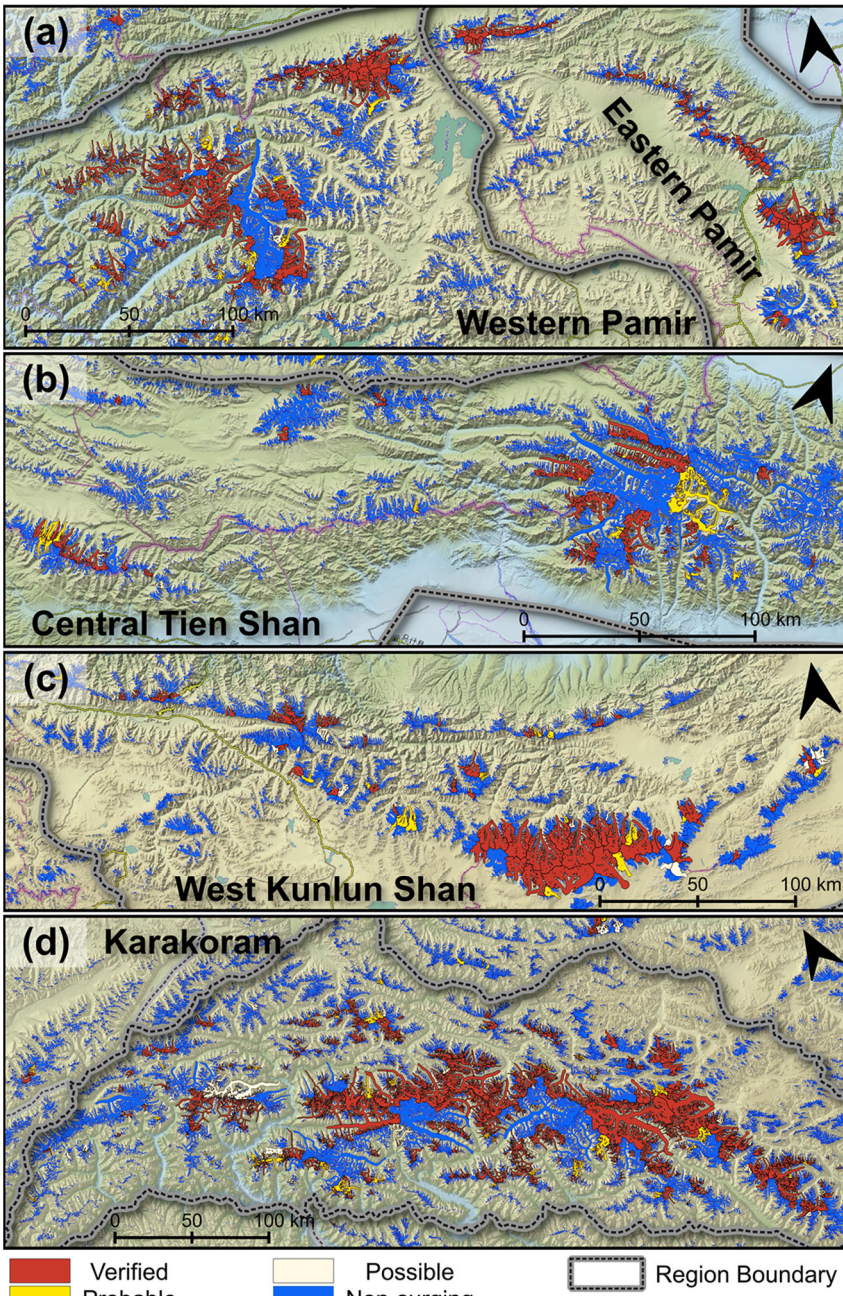
Figure 5: Results of surging glacier identification in (a) the Pamirs, (b) Central Tien Shan, (c) West Kunlun Shan, and (d) Karakoram. The background is the shaded relief of SRTM DEM (Source: USGS).
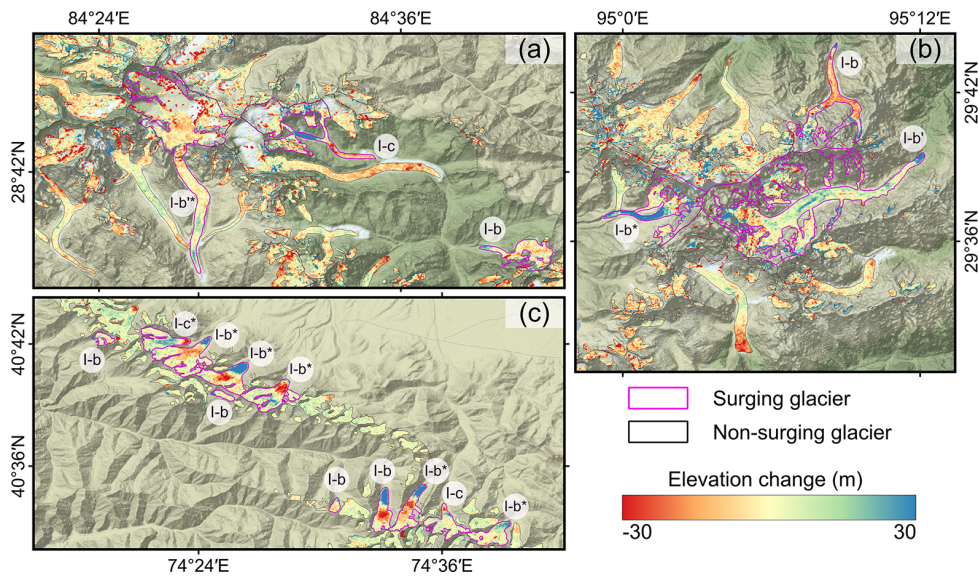
Figure 6: Elevation change map of identified surging glaciers samples in (a) Central Himalaya (1970s-2000), (b) Nyainqentanglha (1970s-2000), and (c) Northern Western Tien Shan (2000-2020). The labels in panels (a) and (b) represent the identified classes based on the elevation change pattern (the criteria of identification are elaborated in section 4.2.1 and Table 1). The subscripts '*' and '′' indicate that the identified class of the glacier is determined by combining morphological changes, and other elevation change maps, respectively. The background is the shaded relief of SRTM DEM (Source: USGS).
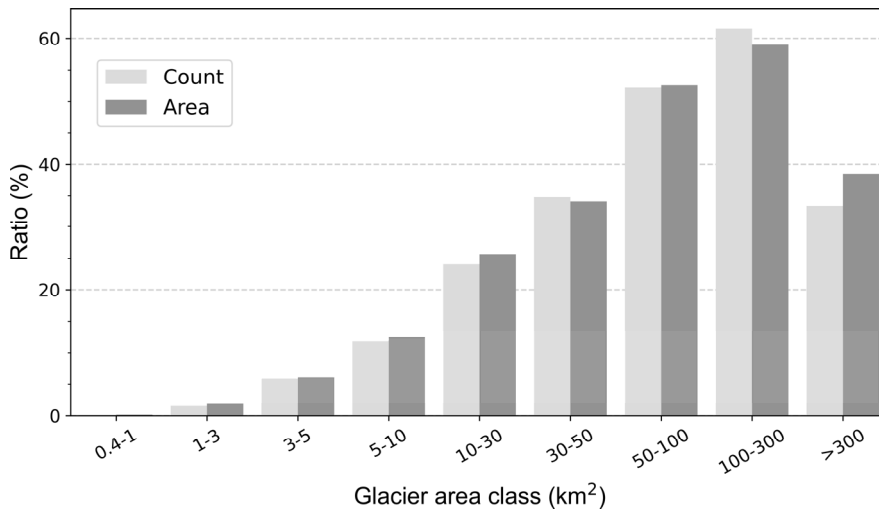
Figure 7: Illustration of the number and area ratios of surging glaciers for different area classes.
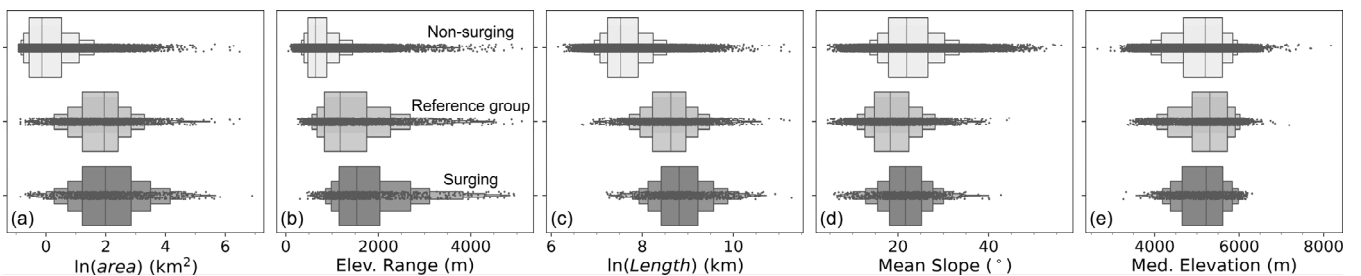
Figure 8: The comparison between the boxplots of geometric properties of non-surging glaciers (top), non-surging glaciers in the reference group (center), and surging glaciers (bottom). (a) Natural logarithm of area, (b) elevation range, (c) Natural logarithm of length, (d) Mean surface slope, (e) Median elevation. Glaciers smaller than 0.4 km² were excluded from the non-surging glacier class.

24
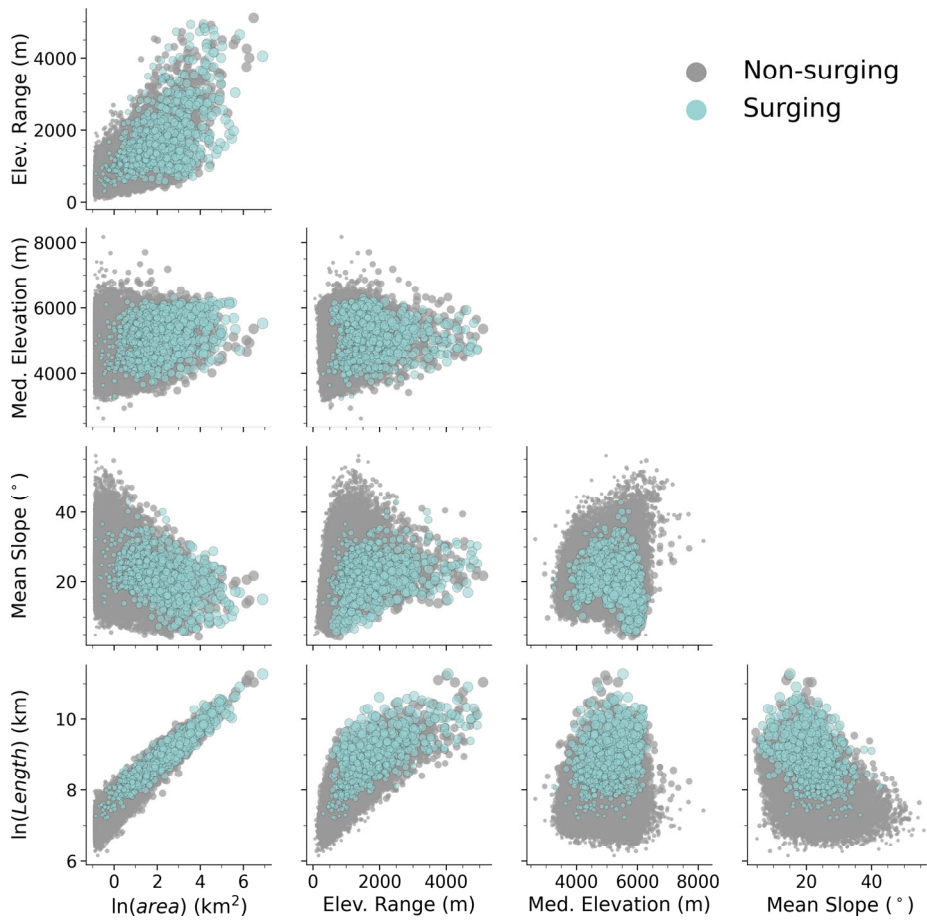
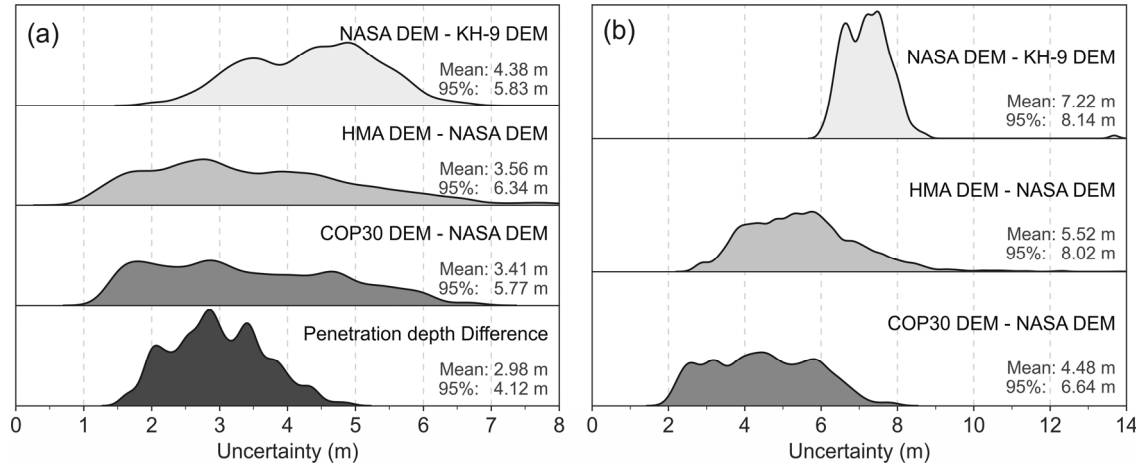Figure 9: Bivariate scatterplots of geometric properties of non-surging and surging glaciers. The larger dots represent larger glaciers. Glaciers smaller than 0.4 km² were excluded in the non-surging glacier class.

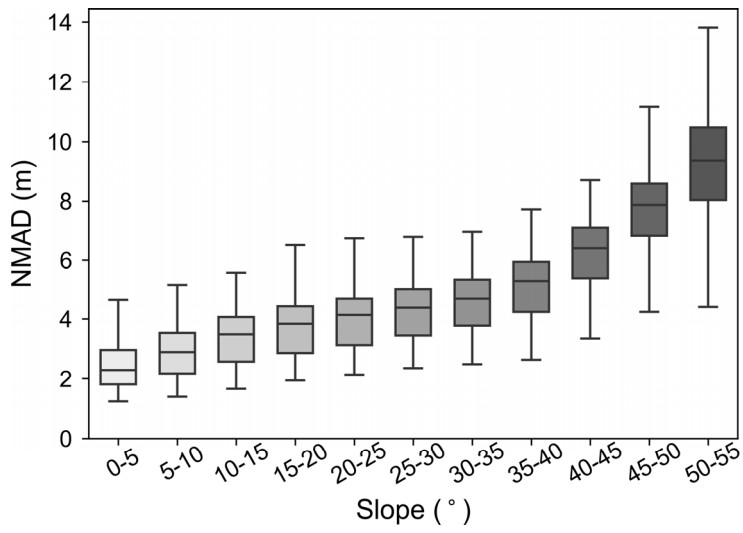Figure 10: The distribution of uncertainties in (a) four kinds of elevation difference observations and (b) three kinds of glacier elevation change observations. In each category, the shaded area denotes the density distribution of the uncertainties in corresponding observations.

Figure 11: The distribution of NMAD of COP30 DEM – NASA DEM difference over stable regions within different slope ranges. The box denotes the interquartile range (IQR, i.e., 75th percentile-25th percentile) in each group. The horizontal line in the box denotes the median value in each group. The upper and lower line represents the range between the minimum value (25th percentile - 1.5IQR) and the maximum value (75th percentile + 1.5IQR).